J. Fluid Mech. (2013), *vol.* 728, *pp.* 239–278. © Cambridge University Press 2013
doi:10.1017/jfm.2013.276

Convective diffusive mixing in concentration polarization: from Taylor dispersion to surface convection

I. Rubinstein and B. Zaltzman†

SIDEER, Blaustein Institutes for Desert Research, Ben-Gurion University of the Negev, Sede-Boqer Campus, 84990, Israel

(Received 4 October 2012; revised 27 April 2013; accepted 26 May 2013; first published online 8 July 2013)

We analyse the steady-state convection–diffusion mixing of a solute by a creeping circulatory flow in a long sealed rectangular two-dimensional channel with impermeable sidewalls and fixed different solute concentrations at the two opposite edges. Solution circulation is due to a constant velocity slip along the sidewalls and a back flow along the channel axis. This simple model distils the essence of circulation in concentration polarization of an electrolyte solution under a DC electric current in a micro-channel sealed by an ion-selective element (a nano-channel or a cation exchange membrane). It is observed that in the slow circulation regime (small *Pe* numbers) the solute flux through the channel is governed by the Taylor–Aris dispersion mechanism, i.e. the flux is driven by the cross-sectional average axial concentration gradient, whereas upon increase in *Pe* this mechanism fails. The general question addressed is where the system goes after the breakdown of the Taylor–Aris dispersion regime. In order to find out the answer, the following specific questions have to be addressed. (1) How does the Taylor–Aris dispersion mechanism break down upon increase in *Pe*? (2) Why does it break down? (3) What is the role of the channel aspect ratio in this breakdown? The answers to these questions are obtained through analysing a hierarchy of suitable auxiliary model problems, including the unidirectional zero discharge channel flow and the circulatory analogue of plane-parallel Couette flow, for which most of the analysis is done. They may be summarized as follows. Upon increase in circulation velocity, the Taylor–Aris dispersion mechanism fails due to the formation of lateral non-uniformities of longitudinal solute concentration gradient driving the dispersion flux. These non-uniformities accumulate in protrusion-like disturbances of the solute concentration (wall fingers) emerging near the channel sidewall at the flow exit from the edge. Wall fingers propagate along the sidewalls with increase in *Pe* and eventually reach the opposite channel edges, transforming into narrow surface convection layers. These layers, together with the edge diffusion layers, form a closed mass transport pattern carrying most of the mass flux through the channel with the bulk largely excluded from the transport. The formation of this pattern finalizes the transition from Taylor–Aris dispersion to the surface convection regime. For large circulation velocities, concentration distribution in the surface convection layers attains an oscillatory spiral structure reminiscent of thermal waves in heat conduction.

Key words: convection in cavities, micro-/nano-fluid dynamics, microfluidics

† Email address for correspondence: boris@bgu.ac.il

https://doi.org/10.1017/jfm.2013.276 Published online by Cambridge University Press

1. Introduction and outline

We analyse the steady-state convection–diffusion mixing of a solute by a creeping circulatory flow in a long sealed rectangular two-dimensional channel (width $2H$, $-H < Y < H$, length $L, 0 < X < L, H < L$) with impermeable sidewalls and fixed solute concentrations at the two edges (zero at the left and unity at the right one). Solution circulation is due to a constant velocity ($-V_0$) slip along the sidewalls and a back flow along the channel axis. At the channel edges no-slip is assumed. The corresponding mathematical model reads

$$\mu\nabla^2\boldsymbol{V} = \boldsymbol{\nabla}P, \quad \boldsymbol{\nabla}\cdot\boldsymbol{V} = 0, \quad \boldsymbol{V}\cdot\boldsymbol{\nabla}c = D_0\nabla^2 c, \tag{1.1a–c}$$

$$c(0, Y) = 0, \quad c(L, Y) = 1, \quad \frac{\partial c}{\partial Y}(X, \pm H) = 0, \tag{1.2a–c}$$

$$\boldsymbol{V}\cdot\boldsymbol{n}|_{X=0,L} = \boldsymbol{0}, \quad \boldsymbol{V}\cdot\boldsymbol{n}|_{Y=\pm H} = \boldsymbol{0}, \tag{1.3a,b}$$

$$U|_{Y=\pm H} = -V_0, \quad W|_{X=0,L} = 0. \tag{1.4a,b}$$

Here, $\boldsymbol{V} = U\boldsymbol{i} + W\boldsymbol{j}$ and P are the dimensional flow velocity and pressure, respectively, whereas c is the dimensionless solute concentration (the only dimensionless variable so far). Equations (1.1*a–c*) are the Stokes, continuity and the convective diffusion equations, respectively; μ is the dynamic viscosity and D_0 is the molecular diffusivity. Boundary conditions (1.2*a–c*) and (1.3*a,b*) prescribe, respectively, the constant solute concentration at the depleted ($X = 0$) and the enriched edges ($X = L$), the walls' impermeability and vanishing of the normal velocity. Equation (1.4*a*) specifies slip velocity at the channel sidewalls, whereas (1.4*b*) specifies the no-slip condition for the flow at the channel edges. For comparison, we will occasionally replace condition (1.4*b*) with the perfect slip condition of the form

$$\left.\frac{\partial W}{\partial X}\right|_{X=0,L} = 0. \tag{1.5}$$

Determination of the flow velocity $\boldsymbol{V}$ is decoupled from that of solute concentration, whereas linearity of the Stokes equation yields the scaling $\boldsymbol{V} = V_0\boldsymbol{v}$, where the dimensionless flow velocity $\boldsymbol{v}$ is a solution to the Stokes/continuity equations (1.1*a,b*) with a unity slip velocity. In figure 1 we present flow streamlines for two values of the aspect ratio, $\varepsilon = H/L$ (our definition of the aspect ratio is reciprocal to the common one for the sake of making ε a small parameter for a long narrow channel).

Formulation (1.1)–(1.4) distils the essence of circulation in concentration polarization of an electrolyte solution under a DC electric current passed from right to left in a micro-channel oriented along the X-axis and sealed at the left end by a cation-selective element, such as a nano-channel or a cation-exchange membrane (Rubinstein & Zaltzman 2000; Rubinstein *et al.* 2002; Zaltzman & Rubinstein 2007; Rubinstein *et al.* 2008; Yossifon & Chang 2008; Mani, Zangle & Santiago 2009; Zangle, Mani & Santiago 2009; Mani & Bazant 2011; Yaroshchuk *et al.* 2011). The term concentration polarization (CP) pertains to variations of the electrolyte concentration forming upon the passage of an electric current from an electrolyte solution into a charge selective solid, such as an electrode, an ion-exchange (electrodialysis) membrane or an array of nano-channels in a microfluidic system. Traditionally, CP was viewed as the main limitation for desalination of saline water by electrodialysis. Recently, in an ingenious modification of electrodialysis, CP has been used as the main desalination mechanism (Kim *et al.* 2010; Bazant *et al.* 2011). A common expression of CP is a characteristic voltage–current curve with a segment in which the current nearly

https://doi.org/10.1017/jfm.2013.276 Published online by Cambridge University Press

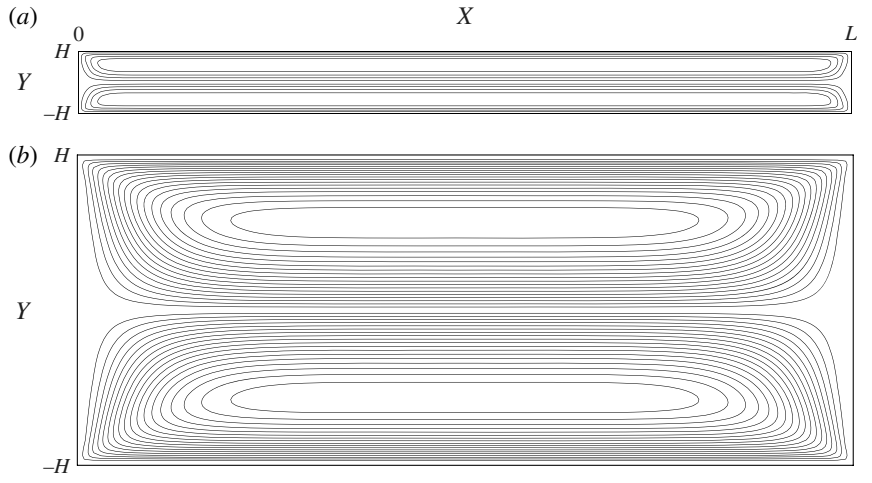


FIGURE 1. Flow streamlines in Poiseuille circulation: (*a*) $\varepsilon = 0.04$, (*b*) $\varepsilon = 0.2$.

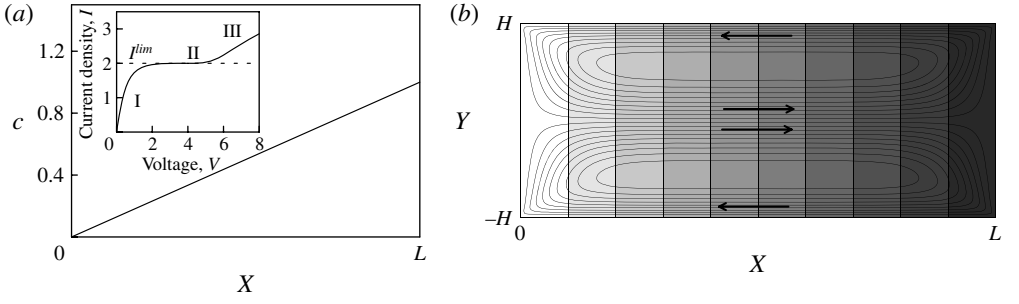


FIGURE 2. Over-limiting current in a micro-channel (typical voltage/current curve in the inset) from a reservoir (right, $X = L$) to a cation-exchange membrane (left, $X = 0$). Linear quiescent concentration profile at the limiting current (*a*) with vanishing concentration at the membrane/solution interface ($X = 0$), to be perturbed by circulation (*b*). Vertical grid lines are the level lines of the unperturbed one-dimensional concentration.

saturates at some plateau value (the limiting current) due to the diffusion limitation associated with CP and the related decrease in interface concentration: see the inset in figure 2(*a*). This segment of voltage–current curve is usually followed by another region of relatively rapid increase in electric current with voltage – the so-called over-limiting conductance regime. The mechanism of over-limiting conductance remained unexplained for a long time. Only recently has it been shown that over-limiting conductance is due to destruction of the diffusion layer by convective-surface-driven mixing that develops spontaneously in the diffusion layer near the charge-selective solid/liquid interface (Rubinstein *et al.* 2002). The source of the underlying flow is electro-osmotic instability (Rubinstein & Zaltzman 2000; Rubinstein *et al.* 2002; Zaltzman & Rubinstein 2007; Rubinstein *et al.* 2008; Yossifon & Chang 2008) related to the formation of the extended space charge (Rubinstein & Shtilman 1979; Rubinstein & Zaltzman 2010) which develops next to the common electric double

https://doi.org/10.1017/jfm.2013.276 Published online by Cambridge University Press

layer in the limiting current/over-limiting conductance regime. This pertains to non-confined systems. Geometric confinement changes the mechanism of over-limiting conductance in CP.

In very shallow micro-channels (depth on a micron/submicron scale) preceding the nano-channel (membrane), over-limiting conductance is associated with the surface conduction effect (Dydek *et al.* 2011). As the micro-channel depth is increased to the tens of microns range, another mechanism – convection due to electro-osmotic flow along the charged channel walls – eventually overtakes the surface conduction. For a dead-end channel sealed by an impermeable membrane, pressure-driven flow develops to oppose electro-osmotic flow and results in the formation of two counter-rotating vortices, which carry concentrated solution to the membrane along the sidewalls and return depleted solution in the centre, as shown in figure 2(*b*). This circulation constitutes the dominant mechanism of over-limiting conductance for the intermediate range of confinements (Dydek *et al.* 2011; Yaroshchuk *et al.* 2011) with aspect ratio in the range $0.01 < \varepsilon < 1$.

The topic of this study is steady-state solute mixing by a circulation of this very kind, relieved from the details of the actual CP (such as electro-osmotic flow velocity dependence on the electric field and solute concentration, resulting in its increase towards the depleted end of the channel). On the other hand, it is closely related to numerous investigations of convection–diffusion mixing by the Taylor–Aris dispersion (TAD), with one difference: most of these investigations for the unreactive systems analyse the time-dependent case, whereas we focus entirely on the steady state (Taylor 1953; Aris 1956). The general question we are asking is how a circulatory flow mixes the linear concentration profile set by the steady-state diffusion and to what extent this mixing can be interpreted in terms of effective diffusivity in the spirit of TAD. Let us precede the formulation of more specific questions with a preliminary discussion.

The gross flow picture in model (1.1)–(1.4), illustrated in figure 1, is independent of V_0 for the creeping flow under consideration and may be described as follows. For small aspect ratio, $\varepsilon \ll 1$ (the case we shall focus on), away from the edges, the fluid flows in a nearly plane-parallel Poiseuille flow with zero discharge (we will refer hereafter to (1.1)–(1.4) as Poiseuille circulation). Near the edges the streamlines turn around and the cross-sectional average transverse velocity W, vanishing at the edge and in the bulk, reaches a maximum at some distance $\Delta \sim H/4$ from the edge. First, let us recall that any convective mixing increases the total mass flux through the channel, $-N_d$, compared to that in quiescent conduction. Indeed, multiplying (1.1*c*) by c and integrating over the area of the channel, using integration by parts and (1.1*b*), (1.2*a–c*), (1.3*a,b*), yields

$$-N_d = D_0 \int_{-H}^{H} \frac{\partial c}{\partial X}(L, Y)\,\mathrm{d}Y = D_0 \iint_{0<X<L,\,-H<Y<H} (\nabla c)^2\,\mathrm{d}X\,\mathrm{d}Y. \tag{1.6}$$

Since the Dirichlet integral on the right-hand side of (1.6) is minimal for c satisfying the Laplace equation, corresponding to zero flow in (1.1*c*), any mixing increases the mass flux. It is our purpose to establish what the regimes and mechanisms of this increase are depending on the range of the Péclet number, $Pe = V_0 H/D_0$, in relation to ε. Let us begin by depicting in figure 3(*a*) the average concentration profiles computed numerically for Poiseuille flow (no-slip) for various Pe. In a practical microfluidic situation Pe may reach values up to 1000 (Chamarthy *et al.* 2008).

https://doi.org/10.1017/jfm.2013.276 Published online by Cambridge University Press

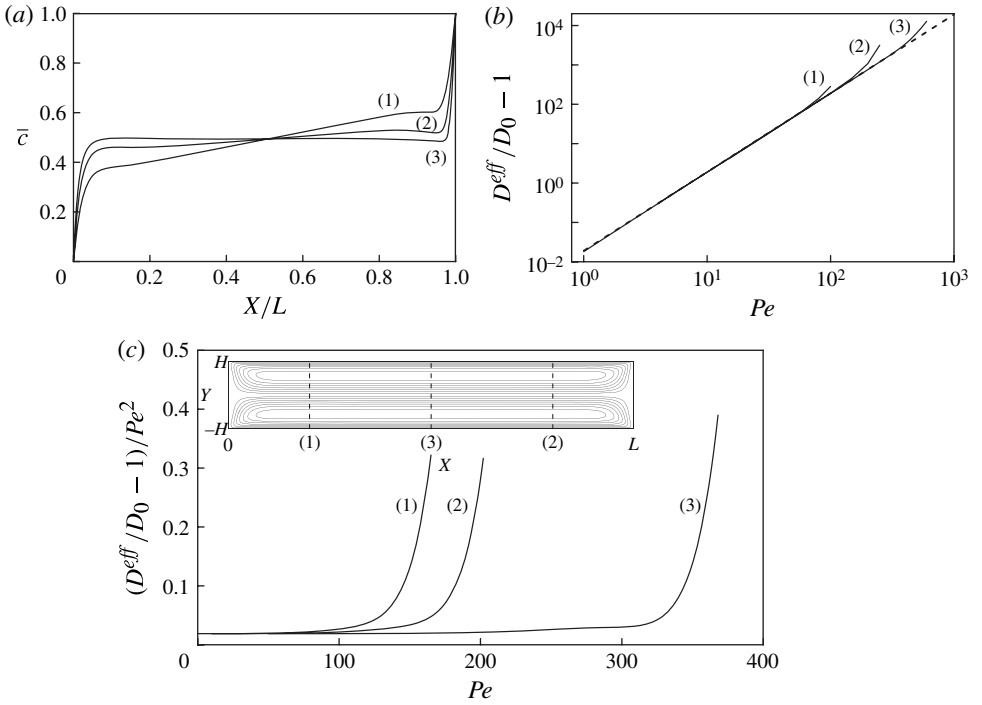


FIGURE 3. (*a*) Cross-sectional average concentration, $\overline{c}(X)$, plots (1) $Pe = 50$, (2) $Pe = 100$, (3) $Pe = 250$, computed for $\varepsilon = 0.1$. (*b*) $D^{eff}/D_0 - 1$ versus Pe in the middle of the channel, computed numerically (solid lines): (1) $\varepsilon = 0.2$, (2) $\varepsilon = 0.08$, (3) $\varepsilon = 0.04$, and predicted by the Taylor–Aris formula $D^{eff}/D_0 - 1 = 2Pe^2/105$ (dashed line). (*c*) Breakdown of TAD along the channel curves (1)–(3) pertaining to the corresponding locations in the inset.

Without addressing at this stage the long-standing debate of whether the concept of TAD dispersion is applicable to a steady state (Balakotaiah & Chang 1995, 2003; Chang & Yeo 2009), let us note that the observed linear average steady-state bulk concentration profile is compatible with the notion of the effective bulk diffusivity D^{eff}, large compared to that in the diffusion layers (molecular diffusivity D_0).

Let us figure out why this should be expected to be the case, and simultaneously, let us recapitulate the basics of the TAD theory (Brenner & Edwards 1993; Stone & Brenner 1999; Chang & Yeo 2009). Let us assume the deviation $c_1(X, Y)$ of the solute concentration from its cross-sectional average, $\overline{c}(X)$, is small; let us assume the longitudinal variations of c_1 compared to the transversal ones are also small. In addition, let both of the small quantities scale with ε. Then, neglecting the contributions quadratic in ε, diffusion equilibrium sets in between the injection of a solute into each cross-section at a rate $U(Y)\partial\overline{c}/\partial X$ per unit area (with a zero total) and the transversal diffusion. In other words, in each cross-section, c_1 is governed by the steady-state transverse diffusion equation with $U(Y)\partial\overline{c}/\partial X$ as a source term, yielding c_1 proportional to $\partial\overline{c}/\partial X$ with a Y-dependent factor proportional to V_0 or, in dimensionless terms, to Pe. This implies, in particular, that without the average concentration gradient $\partial\overline{c}/\partial X$ there would be no c_1, the latter being just a diffusion smeared distortion of $\overline{c}$ by the Y-dependent longitudinal flow with zero average.

https://doi.org/10.1017/jfm.2013.276 Published online by Cambridge University Press

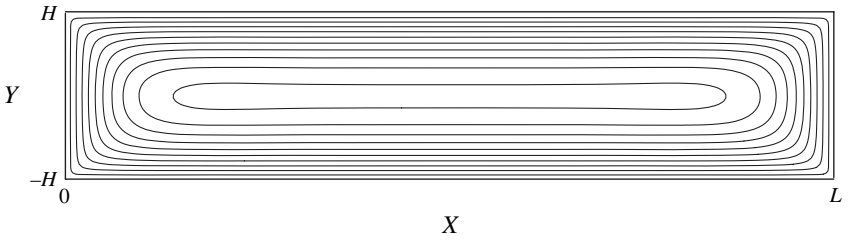


FIGURE 4. Flow streamlines in Couette circulation (perfect slip), $\varepsilon = 0.1$.

Accordingly, in this case there would be no contribution to the overall longitudinal solute flux from the cross-sectional average convective fluctuation flux $\overline{c_1 U}$, that is, no dispersion. In any case, at the steady state, the average longitudinal flux $\overline{c_1 U} - D_0 \partial \overline{c}/\partial X$ is constant along the channel, which implies, taking into account the aforementioned structure of c_1, that $\partial \overline{c}/\partial X$ is constant too. Since U scales with V_0, this reasoning also implies that $\overline{c_1 U}$ is proportional to $\partial \overline{c}/\partial X$ with a proportionality factor in the convective part quadratic in $V_0(Pe)$, in accordance with the TAD theory. It will be shown in § 2 that the assumption of small c_1 is sufficient for TAD to hold, the necessary condition for this being a nearly transversally uniform longitudinal concentration gradient.

As the first step in assessing the extent to which this theory is applicable to our system, we shall for the time being ignore the minor non-monotonicities near the channel edges and focus on the low/moderate velocity (Pe) range which is characterized by a nearly linear bulk average concentration profile (curves (1), (2) in figure 3(a) flanked by two diffusion layers. The effective diffusivity D^{eff} is defined by equating to $-2HD^{eff}\,\partial \overline{c}/\partial X$ the total longitudinal solute flux through a given bulk channel cross-section. According to the TAD theory, D^{eff} should satisfy the relation

$$\frac{D^{eff}}{D_0} - 1 = O(Pe^2). \tag{1.7}$$

In figure 3(b) we compare this prediction with the numerical results for the middle cross-section of the channel in the Poiseuille circulation model. We observe that relation (1.7) indeed holds in our system for a range of Pe which decreases with the increase in aspect ratio ε.

The breakdown of the TAD regime starts near the edges (figure 3c) and propagates toward the centre upon increase in Pe. This start is not symmetric as a result of asymmetry of each of the two 'Poiseuille vortices' with respect to their long central axis. In order to eliminate this asymmetry and deal with a single fully symmetric vortex in the channel, we introduce another flow system in which the slip along the channel sidewalls is directed in opposite directions. This amounts to replacing the slip condition (1.4a) by the condition

$$U|_{Y=\pm H} = \mp V_0. \tag{1.8}$$

In a long narrow channel away from the edges this yields a plane-parallel Couette flow with zero discharge, $U = -YV_0/H$, $W = 0$, (figure 4). The model (1.1)–(1.3), (1.5), (1.8), referred to below as Couette circulation (with perfect slip at the edges), is the simplest of all, almost admitting an analytical treatment. For this reason, we will focus on this model hereafter, with only occasional references to the others.

https://doi.org/10.1017/jfm.2013.276 Published online by Cambridge University Press

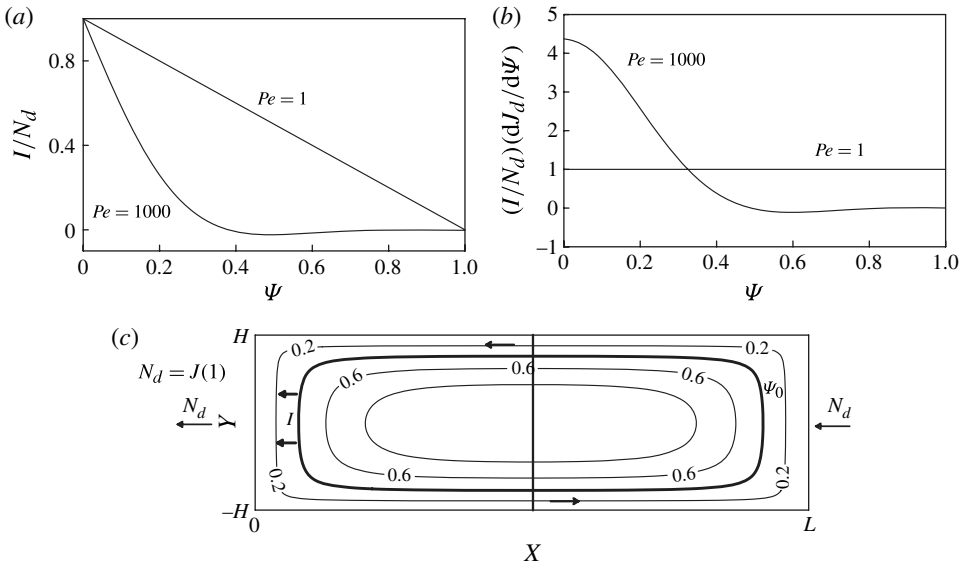


FIGURE 5. Mass flux in channel (Couette circulation, perfect slip, $\varepsilon = 0.05$). (*a*) Flux $-I$ arriving in the stream-tube Ψ from the bulk normalized by the total flux through the channel, $-N$. (*b*) Normalized flux density near streamline Ψ in the middle cross-section. (*c*) Mass balance in the channel. The bold streamline Ψ_0 encompasses the SCLs and the edge diffusion layers, $Pe = 1000$.

Thus, summarizing what has been said so far, up to moderate Pe the steady-state flux through the channel is driven by the axial average concentration gradient through the TAD mechanism. This mechanism fails at large Pe. But how exactly does this happen (question (1) above), and why (question (2)), and what is the role of ε (question (3))? Answering these questions will pave the way to answering the main question of this study: Where does the system go after the breakdown of TAD, that is, what is that state which replaces TAD for large Péclet numbers, and how does the transition between these two states occur (question (0))? Detailed answers to these questions are given in §§ 2–5. Preliminary answers are as follows.

Preliminary answers

Let us focus on the middle cross-section of the channel and draw stream-tubes of various width bordering on the sidewall (figure 5*c*). Let Ψ be the dimensionless stream-function (normalized by the flow discharge through half a channel) vanishing at the wall and equal to unity in the centre. Let us define $-J_d(\Psi)$ as the contribution of a stream-tube Ψ to the total flux $-N_d$ through the channel. Then, $\mathrm{d}J_d(\Psi)/(N_d\mathrm{d}\Psi)$ is the normalized flux density near a given streamline Ψ (figure 5*b*). For small Pe (TAD regime) the flux in the middle cross-section of the channel is distributed among various streamlines with a distribution independent of Pe (in Couette circulation this distribution is nearly uniform). Upon increase in Pe this distribution shifts toward the boundary.

Let us also define $-I(\Psi)$ (figure 5*a*) as the total flux which arrives in the stream-tube Ψ from the bulk. For small Pe (TAD regime) the contribution to the total flux of that arriving from the bulk varies linearly with Ψ. For very large Pe, except for

https://doi.org/10.1017/jfm.2013.276 Published online by Cambridge University Press

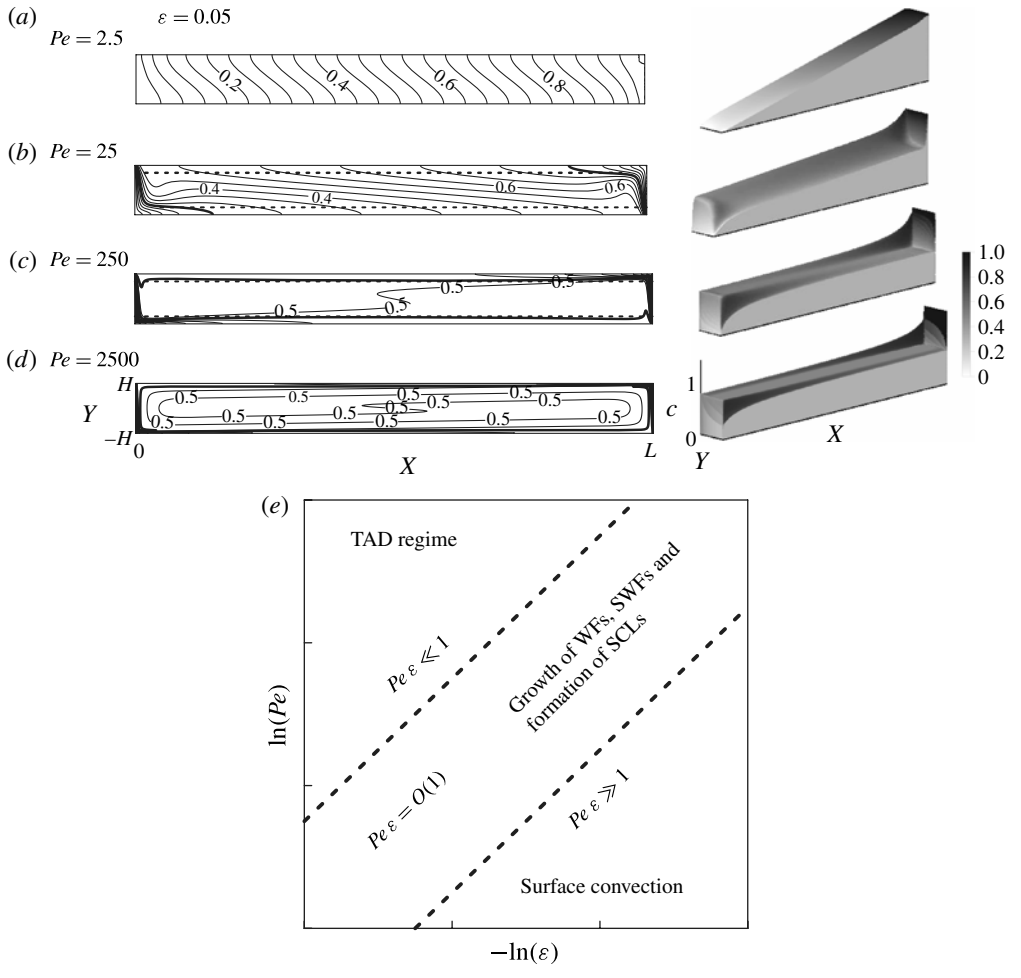


FIGURE 6. (*a*) TAD, (*b*) formation of SWFs, (*c*) development of SCLs, (*d*) spiral pattern in Couette circulation, (*e*) sketch of phase diagram of various transport regimes in the Pe/ε plane.

the stream-tubes passing near the boundary, practically nothing comes from the bulk (figure 5*a*). Thus, for large *Pe*, most of the flux through the channel is carried by a stream-tube passing near the sidewalls and the edges. This tube is largely separate from the bulk, which contributes little to the overall transport through the channel.

The corresponding concentration distribution is depicted in figure 6. We observe that at low/medium circulation velocities (figure 6*a*) the solute mass flux mediated by TAD is relatively uniformly distributed over the streamlines in the channel. In this state, the longitudinal concentration gradient is essentially constant in the channel away from its edges, as reflected by the constant spacing between the concentration level lines in figure 6(*a*). Increase in *Pe* results in the breakdown of the solute mass flux distribution map into a well-mixed bulk, largely excluded from the overall solute transport through the channel, and 'solute jets', passing near sidewalls and transporting most of the solute by convection. These jets, substantial wall fingers (SWFs), are formed by the flow exiting the edge diffusion layers (the regions between

https://doi.org/10.1017/jfm.2013.276 Published online by Cambridge University Press

sidewalls and bold lines in figure 6*b–d*), and, upon increase in *Pe*, propagate in their changing beds, wall fingers (WFs, regions between the sidewalls and the dashed lines in figure 6*b,c*). On reaching the opposite edge (more precisely, the outer edge of its diffusion layer) they transform into separate convective layers (SCLs) (figure 6*c*). These layers at both sidewalls, together with the edge diffusion layers, form a closed mass transport pattern mediating the flux through the channel (figure 6*d*). It will be shown in § 4 that an SCL does not coincide with any particular stream-tube; rather, its significant width increases downstream like that of any diffusion boundary layer.

Thus, the preliminary answers are these: TAD (figure 6*a*) breaks down through the split of the longitudinal transport pattern, uniformly distributed across the channel, into two solute streams carried by the upstream and downstream fluid flows. The scenario is as follows. The exiting flow near a given edge with a fixed concentration value induces a protrusion-like disturbance of the longitudinal solute concentration gradient prescribed by TAD (figure 6*b*). The length of this protrusion, which marks the vicinity of the edge in which TAD fails, is proportional to *Pe* (figure 6*c*). As will be shown in § 2, TAD is destroyed by the emerging non-uniformity of the longitudinal concentration gradient, and an SWF is exactly the place where this non-uniformity is located. A similar finger propagates with increase in *Pe* from the opposite channel edge. When the finger tips cross the middle line, TAD fails in the entire channel. When these tips hit the opposite edges (this happens for $Pe\,\varepsilon \gg 1$), SCLs are formed and the surface convection regime sets in. Upon further increase in *Pe*, the SCL width shrinks as $(Pe\,\varepsilon)^{-1/2}$. This shrinkage is a peculiarity of circulation addressed in § 4, whereas the formation of SWFs and their development into SCLs are elements of a more general scenario for the TAD breakdown. To illustrate this, in § 3 we consider another toy system: zero discharge Couette flow (ZDCF), still with the solute concentrations fixed at the channel edges. This system represents a modification of the common Graetz problem of mass transfer in a multi-pass counterflow laminar mass exchanger (Graetz 1882). In this case too, the TAD regime breaks down through the formation of SCLs developing from the edges. But this time the SCLs are wide, they occupy almost the entire channel, and the longitudinal bulk concentration gradient concentrates in a thin transition layer separating the SCLs. By analysing this latter problem, we recover in § 3 a sequence of known important particular solutions of the convective diffusion equation (Nunge & Gill 1966; Beals 1981, 1985), constituting analogues of the diffusion modes in the Neumann–Dirichlet problem for the Laplace equation distorted by the flow. In this context, the leading mode in this sequence, corresponding to the TAD regime, is an analogue of the linear mode in the solution of that Neumann–Dirichlet problem. While addressing the fine structure of SCLs in circulation in § 5, we encounter a spiral solute concentration pattern (figure 6*d*) – an analogue of the periodic heat wave (Ångström 1861; Carslaw 1921; Samarskii & Tikhonov 1961) – and provide an analytical solution pertaining to this structure. Various transport regimes are schematically summarized in the phase diagram in figure 6(*e*).

2. Lateral uniformity of the longitudinal concentration gradient in TAD

We show in this section that TAD dominates the steady-state mass transport in the bulk of a long plane-parallel channel as long as the relative transversal variation of the

https://doi.org/10.1017/jfm.2013.276 Published online by Cambridge University Press

axial solute concentration gradient is small:

$$\frac{H\displaystyle\int_{-H}^{H}\left|\frac{\partial^2 c}{\partial X\partial Y}\right|\mathrm{d}Y}{\left|\displaystyle\int_{-H}^{H}\frac{\partial c}{\partial X}\mathrm{d}Y\right|}\ll 1. \tag{2.1}$$

In what follows we will employ the following two types of scalings for the spatial variables. Whenever the mass transfer in the entire channel is analysed (as in this section) we will scale X and Y by the channel length L and width H, respectively (scaling 1): $\tilde{x}=X/L$ and $\tilde{y}=Y/H$. On the other hand, to consider the growth of the WFs starting at the channel edges and the beginning of the TAD breakdown resulting from it, we will normalize by the channel width H (scaling 2): $x=X/H$ and $y=Y/H$.

By means of scaling 1, we rewrite the convective diffusion problem (1.1)–(1.3), (1.5), (1.8) in the following dimensionless form:

$$\tilde{\nabla}^2(\tilde{\nabla}^2\tilde{\phi})=0,\quad \tilde{\phi}|_{\tilde{x}=0,1;\tilde{y}=\pm1}=0,\quad \left.\frac{\partial^2\tilde{\phi}}{\partial\tilde{x}^2}\right|_{\tilde{x}=0,1}=0,\quad \left.\frac{\partial\tilde{\phi}}{\partial\tilde{y}}\right|_{\tilde{y}=\pm1}=\mp1, \tag{2.2a–d}$$

$$Pe\left(\varepsilon u\frac{\partial c}{\partial\tilde{x}}+w\frac{\partial c}{\partial\tilde{y}}\right)=\varepsilon^2\tilde{\nabla}^2 c,\quad \left.\frac{\partial c}{\partial\tilde{y}}\right|_{\tilde{y}=\pm1}=0,\quad c|_{\tilde{x}=0}=0,\quad c|_{\tilde{x}=1}=1. \tag{2.3a–d}$$

Here, $\tilde{x}=X/L$, $\tilde{y}=Y/H$, the dimensionless gradient $\tilde{\boldsymbol{\nabla}}$ is defined as $\tilde{\boldsymbol{\nabla}}=\left[\partial/\partial\tilde{x},\,\partial/(\varepsilon\partial\tilde{y})\right]$, $\boldsymbol{v}=(u,w)$ is the dimensionless velocity scaled by the slip velocity V_0, $\tilde{\phi}$ is the dimensionless stream-function, $u=\partial\tilde{\phi}/\partial\tilde{y}$, $w=-\varepsilon\partial\tilde{\phi}/\partial\tilde{x}$.

For the bulk of a narrow channel ($\varepsilon\ll1$), we have

$$|w|\ll1,\quad \tilde{\phi}=\tilde{\phi}(\tilde{y})\quad \text{for } \tilde{x},\,1-\tilde{x}\gg\varepsilon, \tag{2.4}$$

and thus, omitting terms quadratic in ε, elliptic equation (2.3a) yields the parabolic two-way diffusion equation (Beals 1981, 1985):

$$Pe\,\varepsilon u(\tilde{y})\frac{\partial c}{\partial\tilde{x}}=\frac{\partial^2 c}{\partial\tilde{y}^2}\quad \text{for } \tilde{x},\,1-\tilde{x}\gg\varepsilon. \tag{2.5}$$

This equation will be the main mathematical object in our study. In particular, we note the product $Pe\,\varepsilon$ on its left-hand side, which will feature as a major control parameter hereafter, and its related diffusion scaling of the longitudinal variable (in §§ 3 and 4) and of the transversal variable (§ 5). Below we show that, whenever condition (2.1) holds, this equation yields the domination of TAD. Indeed, (2.5) may be rewritten as

$$\frac{\partial^2 c}{\partial\tilde{y}^2}=Pe\,\varepsilon u(\tilde{y})\frac{\mathrm{d}C}{\mathrm{d}\tilde{x}}\left(1+\frac{\partial c/\partial\tilde{x}-\mathrm{d}C/\mathrm{d}\tilde{x}}{\mathrm{d}C/\mathrm{d}\tilde{x}}\right)\quad \text{for } \tilde{x},\,1-\tilde{x}\gg\varepsilon, \tag{2.6}$$

where $C(\tilde{x})$ is the cross-sectional average of the solute concentration,

$$C(\tilde{x})=\frac{1}{2}\int_{-1}^{1}c(\tilde{x},\tilde{y})\,\mathrm{d}\tilde{y}, \tag{2.7}$$

https://doi.org/10.1017/jfm.2013.276 Published online by Cambridge University Press

and the deviation of the longitudinal concentration gradient from its cross-sectional average is evaluated as

$$\left|\frac{\partial c}{\partial \tilde{x}} - \frac{\partial C}{\partial \tilde{x}}\right| = O\left(\int_{-1}^{1}\left|\frac{\partial^2 c}{\partial \tilde{x}\partial \tilde{y}}\right| \mathrm{d}\tilde{y}\right). \tag{2.8}$$

Taking into account the impermeability of the walls at $y = \pm 1$, straightforward integration of this equation across the channel yields along with condition (2.1)

$$c_{\tilde{y}} = \varepsilon Pe\,\tilde{\phi}(\tilde{y})\frac{\mathrm{d}C}{\mathrm{d}\tilde{x}}(\tilde{x})\left[1 + O\left(\frac{\int_{-1}^{1}\left|\partial^2 c/\partial\tilde{x}\partial\tilde{y}\right|\mathrm{d}\tilde{y}}{\mathrm{d}C/\mathrm{d}\tilde{x}}\right)\right]. \tag{2.9}$$

Integrating (2.9) we find

$$c(\tilde{x},\tilde{y}) = C(\tilde{x}) + \varepsilon Pe\left(\int_{-1}^{\tilde{y}}\tilde{\phi}\,\mathrm{d}\tilde{y} - \Phi\right)\frac{\mathrm{d}C}{\mathrm{d}\tilde{x}}(\tilde{x}) \times\left[1 + O\left(\frac{\int_{-1}^{1}\left|\partial^2 c/\partial\tilde{x}\partial\tilde{y}\right|\mathrm{d}\tilde{y}}{\mathrm{d}C/\mathrm{d}\tilde{x}}\right)\right], \tag{2.10}$$

where

$$\Phi = \frac{1}{2}\int_{-1}^{1}\int_{-1}^{\tilde{y}}\tilde{\phi}(s)\,\mathrm{d}s\,\mathrm{d}\tilde{y}. \tag{2.11}$$

Using (2.10) we obtain the following estimate for the density of the axial convective flux as it features in (2.3*a*):

$$\varepsilon Peuc = \varepsilon Pe\frac{\partial\tilde{\phi}}{\partial\tilde{y}}\left(C + \varepsilon\mathrm{Pe}\left(\int_{-1}^{\tilde{y}}\tilde{\phi}\,\mathrm{d}\tilde{y} - \Phi\right)\frac{\mathrm{d}C}{\mathrm{d}\tilde{x}} \times\left[1 + O\left(\frac{\int_{-1}^{1}\left|\partial^2 c/\partial\tilde{x}\partial\tilde{y}\right|\mathrm{d}\tilde{y}}{\mathrm{d}C/\mathrm{d}\tilde{x}}\right)\right]\right). \tag{2.12}$$

Integration of (2.12) across the channel cross-section yields for the overall convective flux the expression

$$J_c(x) = Pe\int_{-1}^{1}\varepsilon uc\,\mathrm{d}\tilde{y} = -(\varepsilon Pe)^2\int_{-1}^{1}\tilde{\phi}^2\,\mathrm{d}\tilde{y}\frac{\mathrm{d}C}{\mathrm{d}\tilde{x}} \times\left[1 + O\left(\frac{\int_{-1}^{1}\left|\partial^2 c/\partial\tilde{x}\partial\tilde{y}\right|\mathrm{d}\tilde{y}}{\mathrm{d}C/\mathrm{d}\tilde{x}}\right)\right], \tag{2.13}$$

https://doi.org/10.1017/jfm.2013.276 Published online by Cambridge University Press

valid in the bulk of our long narrow channel. Accordingly, for the dimensionless counterpart $-N$ of the total flux $-N_d$, (1.6), we have

$$-N = J_c(x) - \varepsilon^2 \frac{\mathrm{d}C}{\mathrm{d}\tilde{x}}$$
$$\approx -\varepsilon^2 \left(Pe^2 \int_{-1}^{1} \tilde{\phi}^2 \, \mathrm{d}\tilde{y} + 1 \right) \frac{\mathrm{d}C}{\mathrm{d}\tilde{x}} \left[1 + O\left(\frac{\int_{-1}^{1} \left| \partial^2 c / \partial \tilde{x} \partial \tilde{y} \right| \mathrm{d}\tilde{y}}{\mathrm{d}C/\mathrm{d}\tilde{x}} \right) \right]. \quad (2.14)$$

The leading-order term in (2.14) constitutes the TAD expression for the solute flux, whereas the requirement of smallness of the correction amounts to inequality (2.1). This latter and the constancy of the overall flux along the channel at the steady state yield

$$\frac{\mathrm{d}C}{\mathrm{d}\tilde{x}} \approx \text{const.} \quad \text{for } \tilde{x},\, 1 - \tilde{x} \gg \varepsilon, \quad (2.15)$$

which implies that $C(\tilde{x})$ is a linear function of $\tilde{x}$.

Thus, in the bulk of a long narrow channel (away from the edges) the TAD mechanism mediates the steady-state mass transfer if and only if the axial derivative of the solute concentration is nearly constant across the channel (condition (2.1)). Simultaneously, we have shown that when this condition holds, the bulk concentration to leading order (see (2.10)) is a superposition of a term linear in $\tilde{x}$ and independent of $\tilde{y}$ with another term solely dependent on $\tilde{y}$. For plane-parallel Couette flow this amounts to

$$c(\tilde{x}, \tilde{y}) = \frac{1}{2} + N_0 \left(\tilde{x} - \frac{Pe\,\varepsilon}{2} \left(\frac{\tilde{y}^3}{3} - \tilde{y} \right) - \frac{1}{2} \right). \quad (2.16)$$

Here, the normalization constant N_0 is specified by the total flux N, (2.14), as

$$N_0 = \frac{15N}{\varepsilon \left(4Pe^2 + 30 \right)}. \quad (2.17)$$

Thus, the partial answer to question (2), i.e. 'why' the TAD mechanism breaks down, is that this is due to the formation of lateral non-uniformity of the axial concentration gradient. Since the concentration in the bulk of the channel obeys the two-way diffusion equation (2.5), the sole source of this non-uniformity is the 'initial' data, that is the deviation of the upstream concentration at the flow exit from the vicinity of the edge from that given by the TAD relation (2.16). To distil the essence of the TAD breakdown upon increase in Pe, we begin with an analysis of mass transfer in ZDCF.

3. Breakdown of TAD in ZDCF and formation of wall fingers

To trace the formation of WFs near the channel edges and the related breakdown of TAD, we scale the spatial variables X and Y by the channel width H:

$$x = \frac{X}{H}, \quad y = \frac{Y}{H}. \quad (3.1)$$

https://doi.org/10.1017/jfm.2013.276 Published online by Cambridge University Press

With this scaling, the boundary value problem for ZDCF assumes the form

$$-Pe\, y\frac{\partial c}{\partial x} = \frac{\partial^2 c}{\partial x^2} + \frac{\partial^2 c}{\partial y^2}, \quad \left.\frac{\partial c}{\partial y}\right|_{\tilde{y}=\pm 1} = 0, \quad c|_{x=0} = 0, \quad c|_{x=1/\varepsilon} = 1. \quad (3.2a\text{–}d)$$

Without the flow ($Pe = 0$), the solution to the problem (3.2*a*,*b*) with a general Dirichlet edge condition instead of (3.2*c*,*d*) is a linear combination of the following 'elliptic' modes:

$$c_0^0 = \frac{1}{2}, \quad c_0^1 = \varepsilon x - \frac{1}{2}, \quad c_n = \exp\frac{\pi n x}{2}\cos\frac{\pi n(y-1)}{2}, \quad n = \pm 1, \pm 2, \ldots. \quad (3.3a\text{–}c)$$

For constant edge values, (3.2*c*,*d*), the concentration $c(x, y)$ is reduced to the superposition of the zero modes, c_0^0, c_0^1. Also, for arbitrary edge conditions at $x = 0, 1/\varepsilon$, the bulk of the channel, $1 \ll |x(1/\varepsilon - x)|$, is dominated by the zero modes c_0^0, c_0^1, with the higher modes present only in the $O(1)$-vicinity of the edges. Next, let us turn to the flow, $Pe > 0$, and consider the distortion of the 'diffusion' modes (3.3*a*–*c*) by convection. Whereas the constant mode c_0^0 remains the same, the linear in x zero-order mode c_0^1 converts to the following superposition of a term linear in x and another one dependent only on y:

$$c_0^0 = \frac{1}{2}, \quad c_0^1 = -\frac{Pe\,\varepsilon}{2}\left(\frac{y^3}{3} - y\right) + \varepsilon x - \frac{1}{2}. \quad (3.4a,b)$$

A suitable linear combination of these two modes forms the Couette TAD solution (2.16). We emphasize that the longitudinal concentration gradient in this solution is identically constant. To construct the higher-order modes ($n = \pm 1, \pm 2 \ldots$), we seek an exponential in x solution of the form

$$c_n = \exp(\gamma_n x) F_n(y). \quad (3.5)$$

The axial symmetry of Couette flow yields

$$\gamma_{-n} = -\gamma_n, \quad F_{-n}(-y) = F_n(y). \quad (3.6)$$

Here γ_n and $F_n(y)$ are subject to determination from the following Sturm–Liouville-type problem:

$$\frac{\mathrm{d}^2 F_n}{\mathrm{d}y^2} + \left(\gamma_n^2 + Pe\gamma_n y\right) F_n = 0, \quad y = \pm 1: \ \frac{\mathrm{d}F_n}{\mathrm{d}y} = 0; \quad F_n(0) = 1, \quad n = \pm 1, \pm 2, \ldots. \quad (3.7a\text{–}c)$$

Here (3.7*c*) is a normalization condition.

In figure 7(*a*), we present the numerically found dependence of the exponent, γ_1, on the Péclet number. We note the non-monotonic character of this dependence. For small Pe we observe increase in γ_1 and a resulting shrinkage of this mode's effect range and the related expansion of the region solely dominated by the leading TAD modes, c_0^0 and c_0^1, (3.4). For Péclet number exceeding a certain critical threshold, the absolute values of the first-order exponents start decreasing until they eventually vanish at large Pe,

$$\gamma_{\pm 1} = O(Pe^{-1}), \quad (3.8)$$

corresponding to the expansion of the region of influence of these modes. The dependence of higher-order exponents, $n = \pm 2, \pm 3 \ldots$, on Pe is similar to that for $n = \pm 1$ with the critical value increasing with n.

https://doi.org/10.1017/jfm.2013.276 Published online by Cambridge University Press

In addition, for a high flow rate, $Pe \gg 1$, it follows from balancing the convective and the longitudinal diffusion terms in (3.2*a*) that the two $1/Pe$-wide boundary layers are formed near the 'inflow' portions of the edges $x = 0, \quad 0 < y < 1$ and $x = 1/\varepsilon, \quad -1 < y < 0$, where the concentrations are imposed differently from those in the incoming flow. In the bulk of the channel, outside these boundary layers, the elliptic problem (3.2*a–d*) and its related spectral problem (3.7) may be simplified by neglecting the longitudinal diffusion. This yields the two-way diffusion problem (recall (2.5)) with the 'initial' concentration specified only on the 'upstream' portion of the edges:

$$-Pe\, y\frac{\partial c}{\partial x} = \frac{\partial^2 c}{\partial y^2}, \quad \left.\frac{\partial c}{\partial y}\right|_{y=\pm 1} = 0, \quad c|_{x=0,-1<y<0} = 0, \quad c|_{x=1/\varepsilon,0<y<1} = 1. \quad (3.9a\text{–}d)$$

We note the singular nature of this problem related to y changing sign on the left-hand side of (3.9*a*) (this is a typical feature of any zero discharge flow). Furthermore, we note the appearance of the x/Pe scaling characteristic of diffusion-like equations. Similarly to (3.4*a,b*), (3.5), we look for a solution to the problem (3.9*a–d*) as a superposition of the TAD solution (3.4*a,b*) and higher-order exponential in x modes:

$$c_n = \exp\frac{\nu_n x}{Pe} G_n(y), \quad (3.10)$$

where, similarly to (3.6),

$$\nu_{-n} = -\nu_n, \quad G_{-n}(-y) = G_n(y). \quad (3.11)$$

Here ν_n and G_n (see figure 7*a,b*) are subject to determination from the following indefinite Sturm–Liouville problem (Beals 1981, 1985):

$$\frac{\mathrm{d}^2 G_n}{\mathrm{d}y^2} + \nu_n y G_n = 0, \quad y = \pm 1: \ \frac{\mathrm{d}G_n}{\mathrm{d}y} = 0, \quad G_n(0) = 1, \quad n = \pm 1, \pm 2 \ldots. \quad (3.12a\text{–}c)$$

Here (3.12*c*) is analogous to (3.7*c*). The problem (3.12) may be solved analytically in terms of Airy functions, which yields the following sequence of real exponents ν_n:

$$\nu_1 \approx -34.3, \quad \nu_2 \approx -112, \quad \nu_3 \approx -234 \ldots. \quad (3.13)$$

The 'parabolic' indefinite Sturm–Liouville problem (3.12) may be viewed as a formal asymptotic limit for $Pe \gg 1$ of the 'elliptic spectral' problem (3.7). Correspondingly, for $Pe \gg 1$, exponents $\gamma_{\pm n}$ are well approximated by their asymptotic counterparts $\nu_{\pm n}$ (see figure 7*a*):

$$\gamma_n \approx \frac{\nu_n}{Pe}, \quad F_n(y) \approx G_n(y) \quad \text{for } Pe \gg 1. \quad (3.14)$$

Each of the aforementioned spectral problems, (3.7*a–c*) and (3.12*a–c*), generates its set of spectral numbers and spectral functions. Half-range completeness of the set (3.4), (3.12) and, correspondingly, solvability of the problem (3.9*a–d*) in terms of the basis functions (3.4), (3.10), has been proved by Beals (1981, 1985). Below we rely on the seminal analysis by Beals (1981, 1985), assuming hereafter $Pe \gg 1$. We are not aware of any rigorous results pertaining to the elliptic formulation (3.7*a–c*).

We represent the solute concentration c in the bulk of the channel (outside the edge boundary layer) as

$$c = \tfrac{1}{2} + N_0 c_0^1 + \Sigma. \quad (3.15)$$

https://doi.org/10.1017/jfm.2013.276 Published online by Cambridge University Press

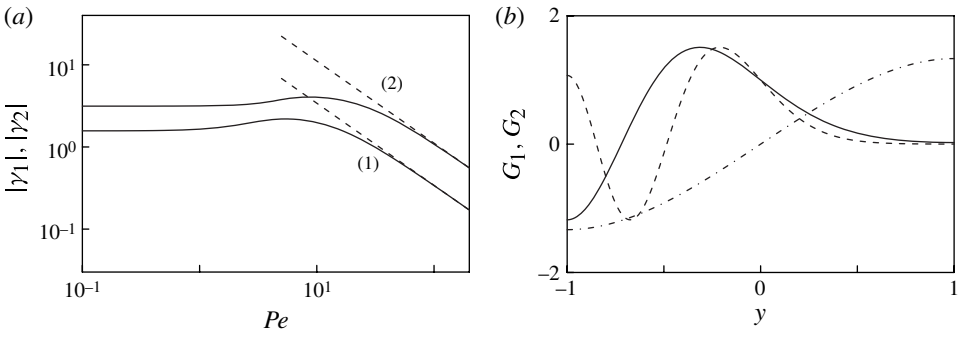


FIGURE 7. Exponential modes in ZDCF. (*a*) (1) $|\gamma_1|$ (solid line), $|\nu_1|/Pe$ (dashed line); (2) $|\gamma_2|$ (solid line), $|\nu_2|/Pe$ (dashed line) versus Pe. (*b*) G_1 (solid line), G_2 (dashed line) and TAD-mode c_0^1 for $Pe\,\varepsilon = 4$ and $x = 1/2\varepsilon$ (dot-dashed line) versus y.

The first two terms in (3.15) stand for the TAD solution, (2.16), and the Σ-term in (3.15) stands for the deviation from TAD at the channel edges. This term may be represented as a sum of exponentially decaying modes (3.10) (Beals 1981, 1985):

$$\Sigma = \sum_{n=1}^{\infty} a_n \exp\frac{\nu_n x}{Pe} G_n(y) - \sum_{n=1}^{\infty} a_n \exp\frac{\nu_n\,(1/\varepsilon - x)}{Pe} G_n(-y). \tag{3.16}$$

Representation (3.15), (3.16) and comparison of 'elliptic' (3.5) and 'parabolic' (3.10) expansions for three values of Pe are illustrated in figure 8 and table 1.

To trace the emergence and development of the longitudinal gradient inhomogeneity we introduce two lines (referred to as 'separatrices' hereafter), $y = l_-(x)$ and $y = l_+(x)$, defined by the zeros of $\partial\Sigma/\partial x$ closest to the walls, where

$$l_-(x) = \min\left\{y < 0 : \frac{\partial c}{\partial x} = N_0\varepsilon\right\}, \quad l_+(x) = \max\left\{y > 0 : \frac{\partial c}{\partial x} = N_0\varepsilon\right\}. \tag{3.17a,b}$$

These lines mark the locations along the channel at which the longitudinal gradient of the concentration deviation from the TAD mode vanishes. Thus, WFs may be defined as the wall portions of the edge perturbation Σ (portion of Σ between the wall and the separatrix: figure 9*a,b*). The symmetry relation (3.11) yields

$$l_+(x) = -l_-(1/\varepsilon - x). \tag{3.18}$$

We note that for $Pe\,\varepsilon \leqslant O(1)$ away from the channel edges expansions (3.16) are dominated by the first-order exponents (figure 9*c*), yielding

$$\Sigma \approx a_1\left(\exp\frac{\nu_1 x}{Pe} G_1(y) - \exp\frac{\nu_1\,(1/\varepsilon - x)}{Pe} G_1(-y)\right). \tag{3.19}$$

This relation yields the following simple implicit equations defining the separatrices in the bulk of the channel:

$$x \approx \frac{1}{2}\left(\frac{Pe}{\nu_1}\ln\frac{-G_1(-l_-)}{G_1(l_-)} + \frac{1}{\varepsilon}\right), \quad x \approx \frac{1}{2}\left(\frac{Pe}{\nu_1}\ln\frac{-G_1(l_+)}{G_1(-l_+)} + \frac{1}{\varepsilon}\right). \tag{3.20a,b}$$

https://doi.org/10.1017/jfm.2013.276 Published online by Cambridge University Press

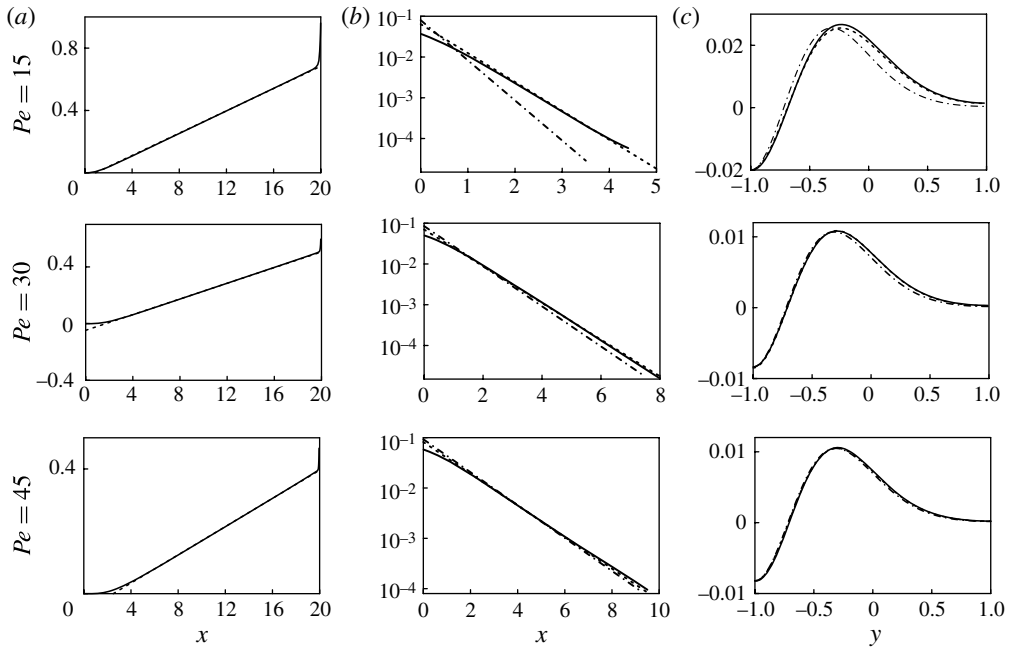


FIGURE 8. Solute concentration in ZDCF (numerical solution of (3.2*a–d*)) for $Pe = 15$, 30, 45, $\varepsilon = 0.05$. (*a*) Wall concentration $c(x, -1)$ (solid line), and the TAD mode in (3.15), $1/2 + N_0 c_0^1(x, -1)$, (dashed line). (*b*) Deviation of the wall concentration from the TAD mode, $c(x, -1) - (1/2 + N_0 c_0^1(x, -1))$ (solid line), first exponential mode in 'elliptic' expansion (3.5), $b_1 \exp(\gamma_1 x) F_1(-1)$ (dashed line), where $\gamma_1 \approx -1.6$ for $Pe = 15$, $\gamma_1 \approx -0.83$ for $Pe = 30$, $\gamma_1 \approx -0.69$ for $Pe = 45$ and the same mode in 'parabolic' expansion (3.10), $a_1 \exp(\nu_1 x/Pe) G_1(-1)$, $\nu_1 \approx -34.3$ (dot-dashed) line. (*c*) The same deviation for the bulk concentration, $-1 < y < 1$ (solid line), and its approximation by the 'elliptic spectral' function $b_1 \exp(\gamma_1 x_0) F_1(y)$ (dashed line), and the 'parabolic spectral' function $a_1 \exp(\nu_1 x_0/Pe) G_1(y)$ (dot-dashed line) near the tip of the SWF (located approximately at $x_0 = 2.5$ for $Pe = 15$, $x_0 = 5$ for $Pe = 30$, and at $x_0 = 6$ for $Pe = 45$).

Substituting $l_\pm = \pm 1$ in the last expression we evaluate the loci of the WFs' tips, and thus the length of the WFs, as

$$x_- \approx \frac{1}{\varepsilon}\left(\frac{1}{2} + 0.113 Pe\,\varepsilon\right), \quad x_+ \approx \frac{1}{\varepsilon}\left(\frac{1}{2} - 0.113 Pe\,\varepsilon\right), \tag{3.21a,b}$$

for the depleted and enriched WFs respectively. (We note the appearance of $Pe\,\varepsilon$ in (3.21*a,b*) in accordance with the comments following (2.5).) Away from the channel edges and the tips of the WFs, relations (3.20*a,b*) yield for the WFs' width the estimates

$$l_-(x) \approx -0.715, \quad l_+(x) \approx 0.715, \tag{3.22a,b}$$

in fairly good agreement with the numerical solution (figure 9*c*).

Thus, a WF is bounded by the channel wall and the separatrix. This latter is a nearly straight line parallel to the wall, $l_\pm = \pm 0.715$, away from the channel edges and the tip of a WF (figure 9*a,b*). This tip propagates with increase in Pe, from the middle of the channel towards the opposite channel edge at a rate proportional to Pe and reaches it for $Pe\,\varepsilon \sim 5$. The magnitude of edge perturbation Σ scales with the TAD solution

https://doi.org/10.1017/jfm.2013.276 Published online by Cambridge University Press

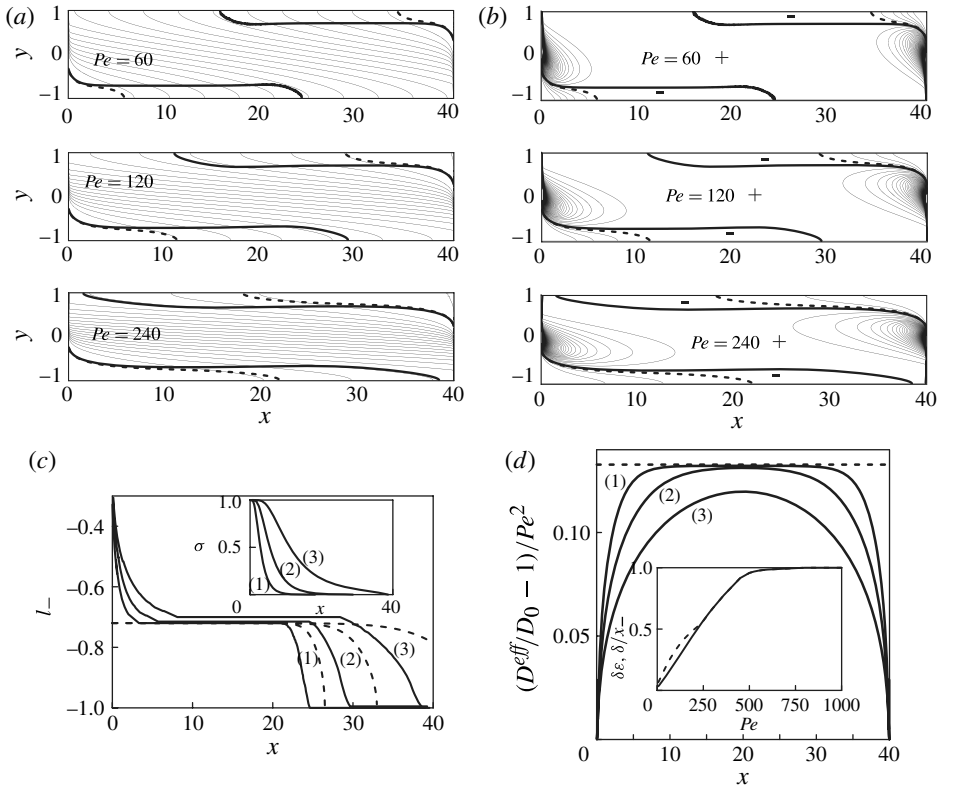


FIGURE 9. WFs, SWFs and the breakdown of TAD in ZDCF for $Pe = 60$, 120, 240 and $Pe\,\varepsilon = 1.5$, 3, 6. (*a*) Maps of solute concentration level lines. (*b*) Level lines of $\partial\Sigma/\partial x$. Bold lines are separatrices marking the WF boundary (level lines, $\partial\Sigma/\partial x = 0$); + positive and − negative deviation of the longitudinal concentration gradient from TAD. Dashed lines mark the SWF boundary. (*c*) Separatrix $l_-(x)$ (solid line) and its analytical counterpart (dashed line): (1) $Pe = 60$ ($Pe\,\varepsilon = 1.5$), (2) $Pe = 120$ ($Pe\,\varepsilon = 3$), (3) $Pe = 240$ ($Pe\,\varepsilon = 6$). Inset: variation along the channel of the ratio of longitudinal edge perturbation gradient, $\partial\Sigma/\partial x(x, -1)$, to that of TAD, $15N/(4Pe^2 + 30)$; (1), (2) and (3) as in the main plot. (*d*) Variation of dimensionless effective diffusivity, normalized by Pe^2, $(D^{eff} - D_0)/(Pe^2 D_0)$, along the channel, for (1) $Pe = 60$, (2) $Pe = 120$, (3) $Pe = 240$; dashed line, the TAD constant $2/15$. Inset: the extent of the SWF relative to the channel length, $\delta\varepsilon$ (solid line), and relative to the WF extent, δ/x_- (dashed line) versus Pe (merging of these two lines at $Pe \approx 250$ means that the WF has reached the channel edge).

ε	Pe	N_0	a_1
0.05	15	0.71	−0.067
0.05	30	0.55	−0.071
0.05	45	0.45	−0.075

TABLE 1. Coefficients of the TAD mode, N_0, and of the first 'parabolic' exponential mode, a_1, numerically computed for the same values of Pe as in figure 8.

https://doi.org/10.1017/jfm.2013.276 Published online by Cambridge University Press

near the channel edges and decays approximately exponentially away from them. The exponential of this decay is proportional to the reciprocal of Pe, and thus increase in Pe yields the expansion of the region in which the longitudinal concentration gradient in a WF ruins TAD. In addition, since the overall flux across the channel is mediated by the TAD term, $N_0 c_0^1$, the edge perturbation Σ only redistributes the flux over the channel cross-section.

Summary

For small Pe, the TAD term, $N_0 c_0^1$, mediates the mass transport practically in the entire channel. WFs are nearly half a channel long (exactly one half for $Pe = 0$) with their substantial portion (SWF) confined to the $O(Pe)$ vicinity of the edges, (3.19). Thus, we define the SWF, emerging at an edge due to incompatibility of the TAD solution with the fixed edge concentration, as the portion of a WF in which the magnitude of perturbation of the longitudinal concentration gradient is no smaller than, say, 90 % of this perturbation. Upon increase in Pe, the SWF grows proportionally to it and so does the WF, with its tip propagating from the middle cross-section of the channel towards the opposite channel edge. Wherever in the channel the SWF reaches, the related non-uniformity of the longitudinal concentration gradient destroys TAD. The WF, broad at its basis near the channel edge due to the effect of the higher-order exponentials, narrows in the bulk of the channel to a strip of nearly constant width. The extent of that base region increases proportionally to Pe too (figure 9*c*). Since the perturbation of the longitudinal concentration gradient by a WF is maximal at the wall, let us characterize an SWF by the ratio σ of this perturbation to the x-derivative of the TAD solution:

$$\sigma(x) = \frac{\left|\dfrac{\partial \Sigma}{\partial x}(x, -1)\right|}{N_0 \varepsilon}. \tag{3.23}$$

In the inset to figure 9(*c*) we depict $\sigma(x)$ for an increasing sequence of Pe. Accordingly, as a measure of the extent of the SWF, δ, let us define that portion of the wall, $0 < x < \delta < x_-$, where $\partial \Sigma / \partial x$ is comparable (for definiteness, larger than the same 90 %) with the x-derivative of TAD and hence is bound to ruin the TAD relation. In the inset to figure 9(*d*) we show that δ grows linearly with Pe and reaches the opposite edge of the channel for Pe roughly twice as large as that for which the finger tip x_- reaches this edge (merging of the continuous and dashed lines). In figure 9(*a,b*) we mark the boundary of the SWF by a dashed line, as opposed to the bold continuous line (separatrix) bounding the WF. Thus, the WF may be viewed as a moving riverbed gradually filled by the propagating SWF, upon increase in Pe. To illustrate the breakdown of TAD (1.7) related to this propagation, we present in figure 9(*d*) the variation of the effective dimensionless diffusivity, D^{eff}/D_0, along the channel:

$$\frac{D^{eff}}{D_0} = 1 + \frac{J_C}{J_D}, \quad J_C = -Pe \int_{-1}^{1} yc(x, y)\, \mathrm{d}y, \quad J_D = -\int_{-1}^{1} \frac{\partial c}{\partial x}(x, y)\, \mathrm{d}y. \tag{3.24}$$

Here $J_C(x)$ and $J_D(x)$ are, respectively, the overall convective and diffusion fluxes through the channel. For TAD, D^{eff}/D_0 equals $2Pe^2/15 + 1$. The deviation from this value in the channel roughly follows the growth of the SWFs.

Finally, for $Pe\,\varepsilon \geqslant O(1)$, the tip of the WF, dominated by the first exponential, reaches the outer edge of the boundary layer at the opposite end of the channel.

https://doi.org/10.1017/jfm.2013.276 Published online by Cambridge University Press

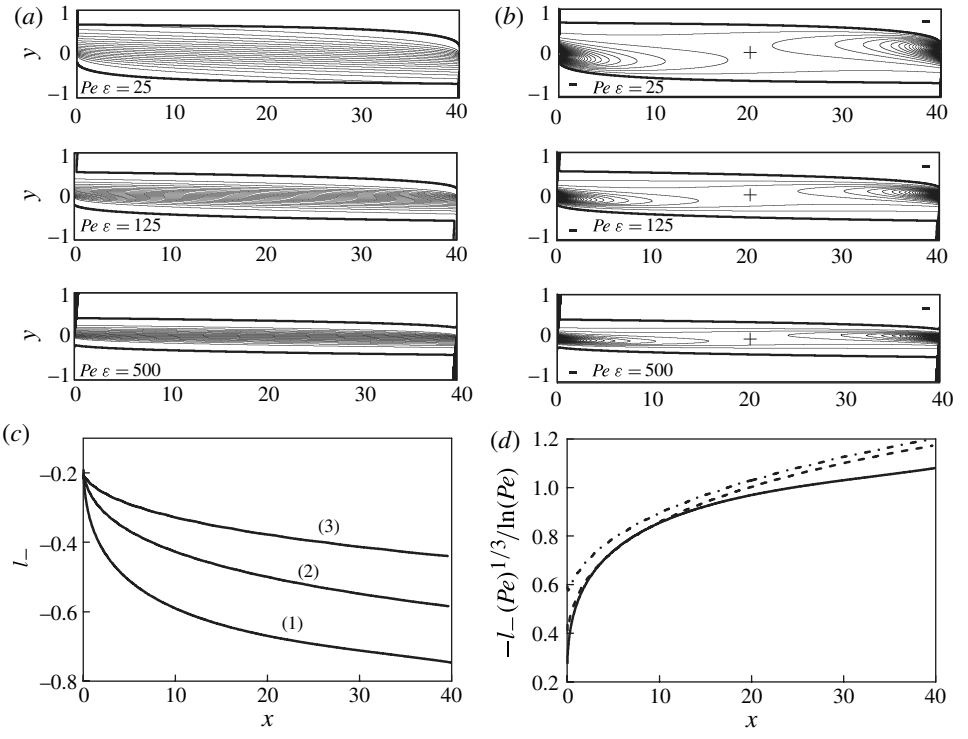


FIGURE 10. Breakdown of TAD and transition to surface convection in ZDCF for $Pe = 1000$, 5000, 20 000 and $Pe\,\varepsilon = 25$, 125, 500. (*a*) Concentration level lines. (*b*) Level lines of $\partial\Sigma/\partial x$. Bold lines are separatrices; level lines, $\partial\Sigma/\partial x = 0$; + positive and − negative deviation of the longitudinal concentration gradient from TAD. (*c*) Separatrix $l_-(x)$: (1) $Pe = 1000$ ($Pe\,\varepsilon = 25$), (2) $Pe = 5000$ ($Pe\,\varepsilon = 125$), (3) $Pe = 20\,000$ ($Pe\,\varepsilon = 500$). (*d*) $Pe^{-1/3}$-scaling for transition layer, normalized separatrices $|l_-(x)|Pe^{1/3}/\ln Pe$: solid line, $Pe = 1000$; dashed line, $Pe = 5000$; dot-dashed line, $Pe = 20\,000$.

Upon further increase in Pe, an increasing number of higher-order exponentials do so. This corresponds to the nearly disappearing x-dependence in the expansions (3.16), resulting in the eventual transfer of the entire 'initial' concentration ($c = 0$ for $y < 0$ and $c = 1$ for $y > 0$) to this edge and the related shift of the separatrices toward the channel axis. This marks the onset of the surface convection regime (figure 10*a,b*). Thus, for $Pe\,\varepsilon \gg 1$, two SCLs, with practically constant 0 and 1 concentration in each, fill the bulk of the channel (figure 10*a*), separated by an $O((Pe\,\varepsilon)^{-1/3})$-wide (figure 10*c,d*) transition layer (this scaling, along with that of edge diffusion boundary layers in circulation, will be discussed in the next section).

Irrespective of the aforementioned details of the emergence and growth of SWFs and their relation to the exponential modes, the main features of the surface convection regime in the ZDCF may be inferred from the following simple scaling arguments. Assuming an order-unity lateral concentration variation in the bulk of the channel, (3.9*a*) yields for the axial variation the estimates

$$\frac{\partial c}{\partial x} = O\left(\frac{1}{Pe}\right), \quad |c\,(1/\varepsilon-, y) - c(0+, y)| \leqslant O\left(\frac{1}{Pe\,\varepsilon}\right) \quad \text{for } y \neq 0, \qquad (3.25)$$

https://doi.org/10.1017/jfm.2013.276 Published online by Cambridge University Press

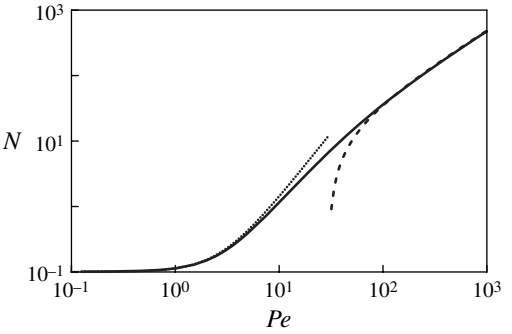


FIGURE 11. Transition from TAD to surface convection in ZDCF. N versus Pe for $\varepsilon = 0.05$ (solid line) and its approximations: by TAD relation, $N = 2\varepsilon\left(2Pe^2/15 + 1\right)$ (2ε, the unperturbed longitudinal concentration gradient, dotted line), and by SCL linear relation, $N = 0.5Pe - 15$ (dashed line).

valid outside the vicinities of the channel axis (where the velocity vanishes) and the edge boundary layers. Thus, for $Pe\,\varepsilon \gg 1$, away from the edges, the solute concentration along the streamlines is nearly constant everywhere in the channel, except in a thin transition layer around the channel axis and the edge boundary layers.

To summarize this section, the following three regimes may be distinguished in ZDCF.

(i) $Pe \leqslant O(1)$: dominance of TAD, that is, efficient averaging by the lateral diffusion of the solute concentration on various streamlines. In terms of the two-way diffusion problem (3.9*a–d*), this implies the dominance of the TAD solution in the bulk of the channel.

(ii) $1 \ll Pe \leqslant O(1/\varepsilon)$: breakdown of the TAD regime through emergence and growth of WFs and SWFs and transition to surface convection. In terms of the two-way diffusion problem (3.9*a–d*), this means coexistence near the channel edges of the TAD solution with exponential modes and emergence of non-uniformity of the longitudinal concentration gradient, propagating along the channel.

(iii) $Pe\,\varepsilon \gg 1$: dominance of surface convection, characterized by a nearly constant solute concentration along the flow streamlines away from the downstream edge boundary layers and negligible transversal diffusion everywhere except for the transition layer around the channel axis. Transition from TAD to surface convection is reflected by the transition from $N \sim Pe^2$ to $N \sim Pe$ dependence of the overall flux $-N$ on Pe characteristic of convective transfer in a layer of finite width with piecewise constant concentration (figure 11).

To illustrate the role of $Pe\,\varepsilon$ as a crucial control parameter, in figure 12(*a*) we present the ZDCF analogue of figure 3(*b*) for the breakdown of the TAD relation for the effective diffusivity, D^{eff}, as a function of Pe (for $\varepsilon = 0.05, 0.1, 0.2$) and of $Pe\,\varepsilon$, observing perfect collapse of the three curves into a single one. In addition, we note the appearance of $Pe\,\varepsilon$ in the N versus Pe dependence depicted in figure 11, inferred by defining the 'effective convective concentration' as $\mathrm{d}N/\mathrm{d}Pe$. In figure 12(*b*) we plot $\mathrm{d}N/\mathrm{d}Pe$ as a function of Pe, for the same three values of ε as in figure 12(*a*), and observe once more a collapse in terms of $Pe\,\varepsilon$.

This scenario of the TAD breakdown and transition to surface convection largely holds for zero-discharge Poiseuille flow as well, with a minor modification of the

https://doi.org/10.1017/jfm.2013.276 Published online by Cambridge University Press

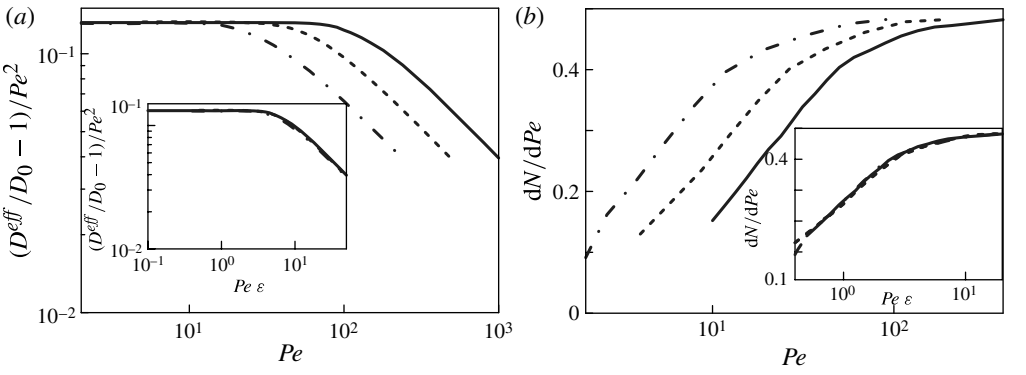


FIGURE 12. Breakdown of TAD and transition to surface convection in ZDCF in terms of $Pe\,\varepsilon$. (*a*) $(D^{eff}/D_0 - 1)/Pe^2$ versus Pe in the middle of the channel for $\varepsilon = 0.05$ (solid line), $\varepsilon = 0.1$ (dashed line), $\varepsilon = 0.2$ (dot-dashed line). Inset: $(D^{eff}/D_0 - 1)/Pe^2$ versus $Pe\,\varepsilon$ for the same values of ε. (*b*) $\mathrm{d}N/\mathrm{d}Pe$ versus Pe for $\varepsilon = 0.05$ (solid line), $\varepsilon = 0.1$ (dashed line), $\varepsilon = 0.2$ (dot-dashed line). Inset: $\mathrm{d}N/\mathrm{d}Pe$ versus $Pe\,\varepsilon$ for the same values of ε.

analysis accounting for the asymmetry of the downstream slip flow and the pressure-driven back flow.

To conclude this section, we note that, with imposed concentration at the edges, $Pe\,\varepsilon > O(1)$ is the universal condition for convection dominance over diffusion. Indeed, the longitudinal convection time T_c is L/V_0, the cross-diffusion time T_d is H^2/D_0, and $Pe\,\varepsilon \gg 1$ simply implies $T_d/T_c \gg 1$, that is, cross-diffusion has no time to average the concentration over various streamlines. In contrast to the commonly expressed view (e.g. Yaroshchuk *et al.* 2011), this alone, in the absence of the edge non-uniformities of the longitudinal concentration gradient propagating along the channel, is not sufficient for breakdown of TAD. Thus, the basic mode, (3.3*a,b*), characterized by a laterally uniform longitudinal concentration gradient, preserves TAD for arbitrarily large Pe, despite large lateral concentration variations and the dominance of convection.

4. Transition to surface convection in circulation

In this section we show how the scenario for the TAD breakdown of the previous section is re-enacted in a circulatory flow. The only difference here is the presence of the diffusion layers near the channel edges (different from $O(Pe^{-1})$-wide boundary layers in ZDCF) and their projections by the flow streamlines onto the channel walls (and the axis, in 'Poiseuille' circulation). For $Pe\,\varepsilon \gg 1$, the entire mass transport through the channel becomes solely mediated by thin SCLs, with an almost completely excluded participation of the bulk.

We begin by considering the formation of edge diffusion layers. The dimensionless width δ_d of these layers is evaluated from the balance of lateral convection terms $Pe\,w\partial c/\partial y$ and longitudinal diffusion terms $\partial^2 c/\partial x^2$ in the dimensionless convection–diffusion equation in the problem

$$Pe\left(u\frac{\partial c}{\partial x} + w\frac{\partial c}{\partial y}\right) = \nabla^2 c, \quad \left.\frac{\partial c}{\partial y}\right|_{y=\pm 1} = 0, \quad c|_{x=0} = 0, \quad c|_{x=1/\varepsilon} = 1, \quad (4.1a\text{–}d)$$

https://doi.org/10.1017/jfm.2013.276 Published online by Cambridge University Press

where u and w are, respectively, the axial and transversal dimensionless velocity components (compare with (3.2*a–d*)). This balance yields

$$Pe\, w\frac{\partial c}{\partial y} \approx \frac{\partial^2 c}{\partial x^2}. \tag{4.2}$$

Estimating the lateral velocity w at the outer edge of the diffusion layer as

$$w = O(\delta_d) \tag{4.3}$$

for no-slip, and

$$w = O(1) \tag{4.4}$$

for the perfect slip condition at the channel edge, we obtain

$$\delta_d \sim Pe^{-1/3} \tag{4.5}$$

for no-slip, and

$$\delta_d \sim Pe^{-1/2} \tag{4.6}$$

for perfect slip. (From identical arguments, (4.5) is also valid for the width of the transition layer between the two bulk SCLs in ZDCF in the previous section.)

Using (4.5), (4.6), we evaluate the overall flux $-N$ through the channel edge as

$$N = O(Pe^{1/3}) \tag{4.7}$$

for no-slip, and

$$N = O(Pe^{1/2}) \tag{4.8}$$

for perfect slip at the channel edges. For small ε, the proportionality constant in (4.5)–(4.8) is independent of ε. In particular, for Couette circulation with perfect edge slip, numerical solution of (4.1*a–d*) yields

$$N \approx 0.7Pe^{1/2}. \tag{4.9}$$

We recall that for ZDCF, N was proportional to Pe. Applying the TAD relation for the effective diffusivity, (2.14), we conclude that as long as the latter holds in the bulk of the channel for $Pe \gg 1$, the axial gradient of the cross-sectional average concentration drops with increase in Pe as $O(N/Pe^2)$, yielding, in accordance with (4.7), (4.8),

$$\frac{\mathrm{d}C}{\mathrm{d}x} = O(Pe^{-5/3}) \tag{4.10}$$

for no-slip, and

$$\frac{\mathrm{d}C}{\mathrm{d}x} = O(Pe^{-3/2}) \tag{4.11}$$

for perfect slip. Thus, in circulation, the bulk mixing is more efficient with no-slip at the edges compared to perfect slip, and so is the mixing in circulation compared to that in ZDCF, for which

$$\frac{\mathrm{d}C}{\mathrm{d}x} = O(Pe^{-1}). \tag{4.12}$$

We limit ourselves to these order-of-magnitude estimates, omitting from this paper detailed analysis of the edge diffusion layers and their matching to the bulk. Most

https://doi.org/10.1017/jfm.2013.276 Published online by Cambridge University Press

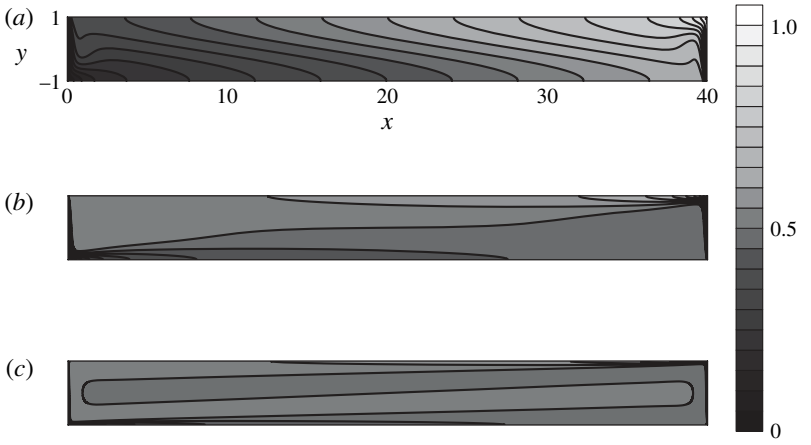


FIGURE 13. Concentration level lines in Couette circulation for (*a*) $Pe = 25$, (*b*) $Pe = 200$, (*c*) $Pe = 1000$.

results in the rest of this section are based on the numerical solution of problem (4.1) and its interpretation in terms of Beals' basis expansion.

We begin by tracing the formation of WFs, SWFs and SCLs and the transition from TAD to surface convection in circulatory Couette flow with perfect edge slip. We note that due to the plane-parallel character of the flow away from the edges (figures 1 and 4), (3.9*a*) is still valid. What has to be changed is the initial condition (3.9*c,d*), which is replaced by that for the upstream concentration at the exit from the edge diffusion layer. This concentration is the projection by the flow of the edge diffusion layer concentration profile onto the vicinity of the channel wall (figure 13*b,c*). In figure 14 we verify the validity of representation (3.15), (3.16) of solute concentration for a circulatory flow through the Beals (3.4), (3.11) basis expansion of the numerical solution to the problem (4.1*a–d*) and observe that, in accordance with the order of magnitude estimates, (4.10), (4.11), the rate of bulk mixing is higher in circulation compared to ZDCF, (4.12); in addition, the breakdown of TAD near the edge in the exiting flow sets for smaller Pe in circulation (compare figures 8*a* and 14*a* and the numerically computed first exponential, a_1, in tables 1 and 2). Next, in figure 15 we plot the concentration level lines (figure 15*a*) and the deviation of the concentration longitudinal gradient from that predicted by the TAD solution (figure 15*b*) together with separatrices $l_-(x)$ (figure 15*c*) and variation of the effective diffusivity along the channel for Pe in the range $O(1) \leqslant Pe \leqslant O(\varepsilon^{-1})$, corresponding to the emergence and growth of SWFs (figure 15*d*).

The results in figure 15 pertaining to the development of WFs and SWFs are similar to those for ZDCF (figure 9) with only one difference: in circulation, the 'initial' edge perturbation $\partial\Sigma/\partial x$ is a projection by the flow of the high concentration gradient in the diffusion layer onto the channel wall; as a result, a WF is 'initially' confined to the vicinity of the wall, rather than distributed over the edge. Accordingly, the approximate bulk separatrices, $l_\pm \approx \pm 0.715$, are approached from the side of the wall rather than from the bulk as before. In this relation, it is instructive to compare figure 15(*c*) in detail with its ZDCF analogue, figure 9(*c*). In the latter, the edge deviation of $l_-(x)$

https://doi.org/10.1017/jfm.2013.276 Published online by Cambridge University Press

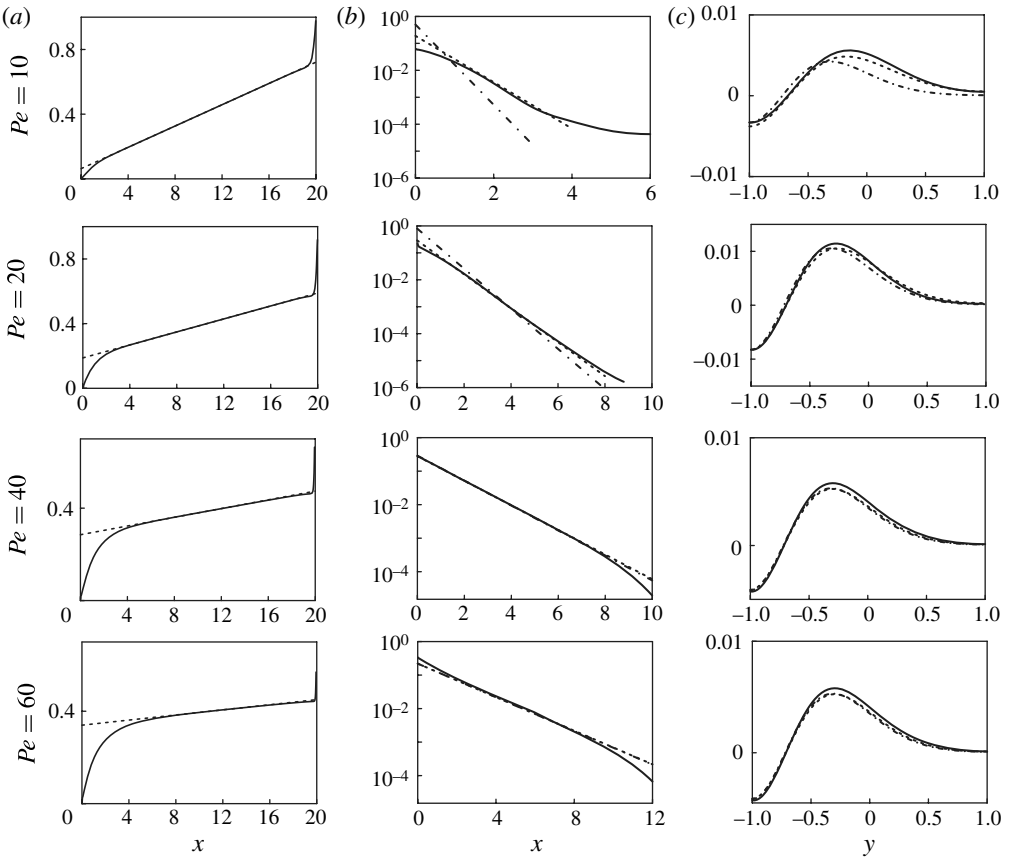


FIGURE 14. Solute concentration in Couette circulation for $Pe = 10, 20, 40, 60$. (*a*) Wall concentration $c(x, -1)$ (solid line), and TAD mode, $1/2 + N_0 c_0^1(x, -1)$ (dashed line). (*b*) Deviation of the wall concentration from the TAD solution, $c(x, -1) - (1/2 + N_0 c_0^1(x, -1))$ (solid line), first exponential mode in 'elliptic' expansion (3.5), $b_1 \exp(\gamma_1 x) F_1(-1)$ (dashed line), where $\gamma_1 \approx -1.98$ for $Pe = 10$, $\gamma_1 \approx -1.4$ for $Pe = 20$, $\gamma_1 \approx -0.825$ for $Pe = 40$, $\gamma_1 \approx -0.57$ for $Pe = 40$ and the same mode in 'parabolic' expansion (3.10), $a_1 \exp(\nu_1 x/Pe) G_1(-1)$, $\nu_1 \approx -34.3$ (dot-dashed) line. (*c*) The same deviation for the bulk concentration, $-1 < y < 1$ (solid line), and its approximation by the 'elliptic spectral' function $b_1 \exp(\gamma_1 x_0/Pe) F_1(y)$ (dashed line), and the 'parabolic spectral' function $a_1 \exp(\nu_1 x_0/Pe) G_1(y)$ (dot-dashed line) near the tip of the SWF (where higher-order modes, $n = 2, 3 \ldots$, have already vanished) located approximately at $x_0 = 2$ for $Pe = 10$, $x_0 = 3.5$ for $Pe = 20$, $x_0 = 5$ for $Pe = 40$, and $x_0 = 6$ for $Pe = 60$.

from its leading-order asymptotic value, -0.715, starts from the channel axis and, upon increase in Pe, propagates into the bulk. Eventually, this results in widening of the WF and SWF, illustrated in figure 10(*c,d*), until an SCL nearly half a channel wide is formed. In contrast, in the circulation addressed in figure 15, near the edge $l_-(x)$ first approaches the channel sidewall, $y = -1$, the approach being closer for larger Pe, and only then starts tending towards its asymptotic value from below, -0.715. Upon further increase in Pe, this 'narrow' portion of the WF reaches the opposite channel edge, yielding the formation of a $Pe^{-1/2}$-wide SCL as illustrated in figure 15(*c*).

https://doi.org/10.1017/jfm.2013.276 Published online by Cambridge University Press

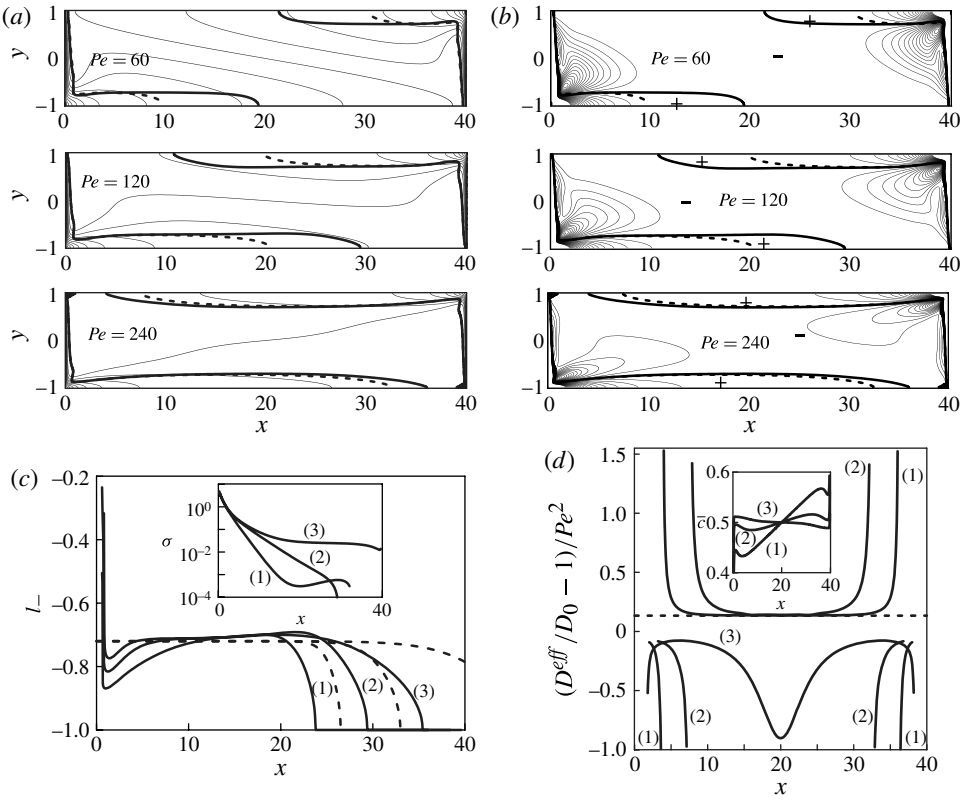


FIGURE 15. WFs, SWFs and the breakdown of TAD in Couette circulation for $Pe = 60, 120, 240$ and $Pe\,\varepsilon = 1.5, 3, 6$. (*a*) Concentration level lines. (*b*) Level lines of $\partial\Sigma/\partial x$. Bold lines are separatrices marking the WF boundary; level lines, $\partial\Sigma/\partial x = 0$; + positive and − negative deviation of the longitudinal concentration gradient from TAD. Dashed lines mark the SWF boundary. (*c*) Separatrix $l_-(x)$ (solid line) and its analytical counterpart (dashed line): (1) $Pe = 60$ ($Pe\,\varepsilon = 1.5$), (2) $Pe = 120$ ($Pe\,\varepsilon = 3$), (3) $Pe = 240$ ($Pe\,\varepsilon = 6$). Inset: variation along the channel of the ratio of longitudinal edge perturbation gradient, $\partial\Sigma/\partial x$, to that of TAD, $N_0\varepsilon$; (1), (2) and (3) as in the main plot. (*d*) Variation along the channel of dimensionless effective diffusivity normalized by Pe^2, $(D^{eff} - D_0)/(Pe^2 D_0)$, for (1) $Pe = 60$, (2) $Pe = 120$, (3) $Pe = 240$; dashed line, the TAD constant 2/15. Inset: cross-sectional average concentration profiles, $\bar{c}(x)$: (1), (2) and (3) as in the main plot (*d*).

ε	Pe	N_0	a_1
0.05	10	0.66	−0.42
0.05	20	0.40	−0.67
0.05	40	0.19	−0.24
0.05	60	0.11	−0.18

TABLE 2. Coefficients of the TAD mode, N_0, and of the first 'parabolic' exponential mode, a_1, numerically computed for the same values of Pe as in figure 14.

https://doi.org/10.1017/jfm.2013.276 Published online by Cambridge University Press

To summarize, for Pe in the range $O(1) \leqslant Pe \leqslant O(\varepsilon^{-1})$, corresponding to the emergence and growth of the WFs in circulation, the larger is Pe and the thinner is the edge diffusion layer, the closer to the edge the first exponential mode starts to dominate the deviation of the wall concentration from TAD (figure 14*b*). Upon further increase in Pe, in the immediate proximity of the edge, higher exponential modes start interfering with the first mode, pushing the region in which it dominates away from the edge (figure 14*b*, $Pe = 40$ and $Pe = 60$). For sufficiently large Pe, away from the edges, Σ is well approximated by the first exponential mode (figure 14*c*), whose amplitude for a circulatory flow is an order of magnitude larger than that for the channel flow (compare first exponential coefficients, a_1, in tables 1 and 2). In WFs ($-1 < y < l_-(x)$ for the depleted edge, $x = 0$, and $l_+(x) < y < 1$ for the enriched edge, $x = 1/\varepsilon$) the leading-order exponential mode enhances the longitudinal concentration gradient (figure 15*b*), whereas in the rest of the channel bulk ($l_-(x) < y < 1$ for the depleted edge $x = 0$ and $-1 < y < l_+(x)$ for the enriched edge $x = 1/\varepsilon$), it reduces it and even reverses its sign. This results in the vanishing and eventual sign-reversal of the cross-sectional average longitudinal solute concentration gradient in the vicinity of the channel edge, the vicinity increasing with Pe, and eventually in the entire channel (inset to figure 15*d*), and the related change of sign of the effective diffusivity for large Pe (figure 15*d*). This non-monotonicity also manifests itself in the two-dimensional maps of the level lines of solute concentration (figure 15*a*). Recall that, away from the channel edges, the overall flux across the channel,

$$N = -\int_{-1}^{1} Pe\, yc\, \mathrm{d}y - \int_{-1}^{1} \frac{\partial c}{\partial x}\, \mathrm{d}y, \tag{4.13}$$

is mediated by the TAD mode c_0^1 only, which implies, in accordance with (3.15),

$$-Pe \int_{-1}^{1} y\Sigma \mathrm{d}y - \int_{-1}^{1} \frac{\partial \Sigma}{\partial x} \mathrm{d}y = 0. \tag{4.14}$$

Neglecting the contribution of longitudinal diffusion away from the channel edges in (4.14) yields

$$\int_{-1}^{1} y\Sigma\, \mathrm{d}y = 0. \tag{4.15}$$

Differentiation of (4.15) in x results in

$$\int_{-1}^{1} y \frac{\partial \Sigma}{\partial x}\, \mathrm{d}y = 0, \tag{4.16}$$

holding everywhere except the immediate vicinity of the edges where the flow in y-direction is non-negligible. Equation (4.16) implies that the WFs carrying a positive longitudinal gradient and occupying the area between the walls and separatrices are balanced by the bulk lying between the separatrices (figure 15*b*), in which the longitudinal gradient is negative. Since the flow velocity decreases towards the channel axis, the effect of this bulk on the cross-sectional average concentration gradient prevails over that of the WFs. Thus, while Σ does not affect the overall cross-sectional average flux, it strongly affects the cross-sectional average concentration gradient. In particular, for a circulatory flow, in a vicinity of the edges increasing with Pe, the local

https://doi.org/10.1017/jfm.2013.276 Published online by Cambridge University Press

diffusion counteracts the overall dispersion. This increases the average concentration gradient near the middle cross-section, thus impeding the overall mixing (inset to figure 15*d*). Eventually, upon increase in Pe, the sign of effective diffusivity is reversed in most of the channel, corresponding to the dramatic change from curves (1) and (2) to (3) in figure 15(*d*). Finally, we note from a comparison of figures 9(*b*) and 15(*b*) that this effect is absent in ZDCF, where D^{eff} preserves its sign, with the longitudinal concentration gradient mostly confined to the transition layer around the channel axis.

Next, let us trace the growth of WFs and SWFs, their transformation into SCLs and the related transition to surface convection upon Pe increasing from the range $O(1) < Pe \leqslant O(\varepsilon^{-1})$ to $Pe > O(\varepsilon^{-1})$. In this range, according to (2.16), (2.17), (4.8), the TAD solution is close to the average concentration, 1/2. Due to the $Pe^{-1/2}$-shrinkage of the stream-tube spanning the diffusion layer, the 'initial data' for the two-way diffusion (3.9*a*) may be approximated by the Dirac δ-function, implying a zero 'initial' width of WFs. For Pe in the range $O(1) < Pe \leqslant O(\varepsilon^{-1})$, the higher-order exponentials in Σ expansion decay away from the channel edge; correspondingly, the WF broadens into a fixed-width strip bounded by the wall and the first exponential dominated bulk separatrix, $l_{\pm} \approx \pm 0.715$. As in ZDCF, for $Pe\,\varepsilon \gg 1$ the tip of a WF dominated by the first exponential reaches the opposite end of the channel and, upon further increase in Pe, an increasing number of higher-order exponentials do so, signalling the transformation of the WF into an SCL. Whereas in ZDCF this amounted to the transfer of the fixed 'initial' concentration to the opposite channel edge, for a circulatory flow, due to the shrinking support of the edge perturbation, the effect of higher exponentials is different. To trace it, we plot in figure 16 the concentration level lines (figure 16*a*) together with those of $\partial\Sigma/\partial x$ (figure 16*b*), along with separatrices for an increasing sequence of $Pe\,\varepsilon$ (figure 16*c,d*). We note that in the range $Pe\,\varepsilon \gg 1$ the SCL is dominated by the $(Pe\,\varepsilon)^{-1/2}$-scale, and by moving away from the channel edge it broadens as $\sqrt{x}$ (figure 16*d*). The emergence of this dependence may be rationalized via the following simple argument. The negligible smallness of the lateral velocity variation in (3.9*a*), together with the shrinkage of the support of the 'initial' perturbation of laterally constant longitudinal gradient in the vicinity of the channel walls for $Pe \gg 1$, yields the approximate impulse response solution

$$c \approx \frac{1}{2} + N \begin{cases} -\sqrt{\dfrac{1}{4Pe\,\pi x}}\,\mathrm{e}^{-Pe(y+1)^2/4x}, & 0 \leqslant y+1 \ll 1, \\ \sqrt{\dfrac{1}{4Pe\,\pi\left(\dfrac{1}{\varepsilon}-x\right)}}\,\mathrm{e}^{-Pe(y-1)^2/4(1/\varepsilon-x)}, & 0 \leqslant 1-y \ll 1. \end{cases} \tag{4.17}$$

The impulse response solution (4.17) is valid for this vicinity of the channel walls for $Pe \gg 1$ and in the entire channel for $Pe\,\varepsilon \gg 1$ (figure 17*d*). Substituting (4.17) in (3.17) and keeping the leading-order terms yields for $Pe\,\varepsilon \gg 1$

$$l_-(x) \approx -1 + \sqrt{\frac{2x}{Pe}}, \quad l_+(x) \approx 1 - \sqrt{\frac{2\left(\dfrac{1}{\varepsilon}-x\right)}{Pe}}, \tag{4.18}$$

https://doi.org/10.1017/jfm.2013.276 Published online by Cambridge University Press

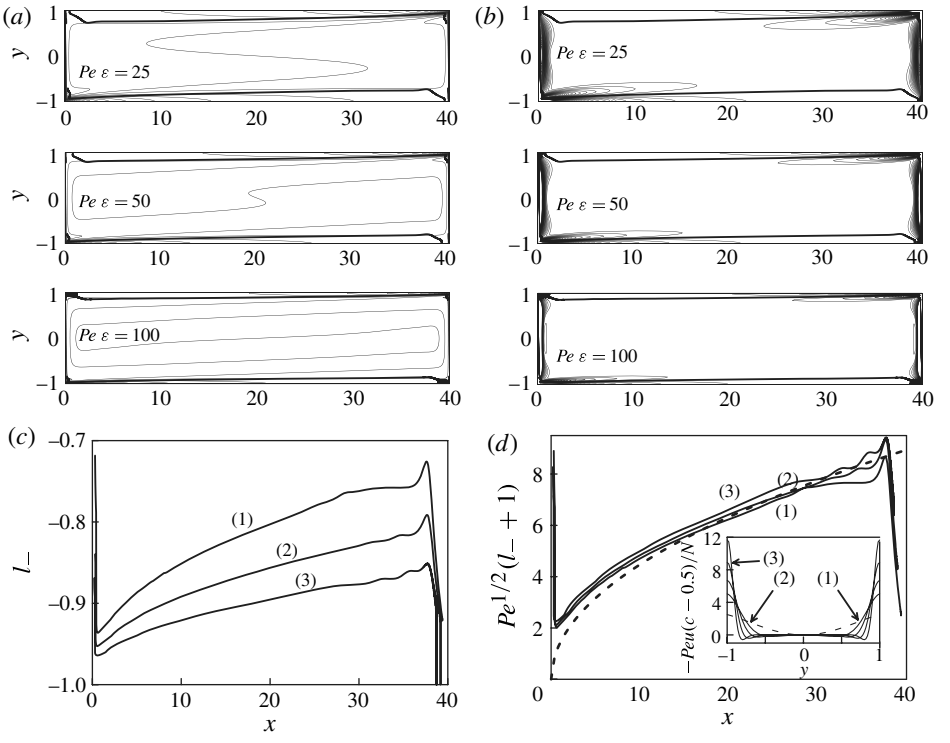


FIGURE 16. Breakdown of TAD and transition to surface convection in Couette circulation for $Pe = 1000, 2000, 4000$ and $Pe\,\varepsilon = 25, 50, 100$. (*a*) Concentration level lines. (*b*) Level lines of $\partial\Sigma/\partial x$. Bold lines are separatrices; level lines, $\partial\Sigma/\partial x = 0$. (*c*) Separatrix $y = l_-(x)$: (1) $Pe\,\varepsilon = 25$, (2) $Pe\,\varepsilon = 50$, (3) $Pe\,\varepsilon = 100$. (*d*) $Pe^{1/2}$-scaling for the SCL, normalized separatrices $y = (l_-(x) + 1)Pe^{1/2}$; (1), (2) and (3) as in (*c*); dashed line, approximation $y = \sqrt{2x}$. Inset: lateral variation of normalized flux density, $Pe\,u(c - 0.5)/N$, in the middle cross-section of the channel, $x = 1/2\varepsilon$ (solid line), the same for the TAD solution (dashed line).

in fairly good agreement with the numerical solution (figure 16*d*). In addition to recovering the $\sqrt{x}$-law, (4.18) reveals the $Pe^{-1/2}$-scale to be the one dominating the width of the WFs (separatrices $l_\pm$) whenever all exponential modes coexist. The moment they fill the entire channel length, the WF converts to an SCL, an $O((Pe\,\varepsilon)^{-1/2})$-wide surface convective layer (figure 16), signalling the transition to the surface convection regime outlined in the Introduction (figures 5 and 6). We remind the reader that the WF first emerged as an $O(Pe^{-1/2})$-wide projection of the edge diffusion layers, developed into a strip of finite width ($l_\pm \approx \pm 0.715$), and, subsequently, upon its tip reaching the opposite channel edge, shrank to the $O((Pe\,\varepsilon)^{-1/2})$-width. To illustrate the validity of SCL-approximation (4.18) for the entire range of $\varepsilon \ll 1$, in figure 17(*a*) we compare, for $\varepsilon = 0.025, 0.5, 0.1$, the numerically calculated separatrices $l_-(x)$ with their approximation (4.18). In the inset to figure 17(*a*), we illustrate (by introducing the normalized longitudinal variable $x\varepsilon$) the scaling of the SCL-width by $(Pe\,\varepsilon)^{-1/2}$, valid for $Pe\,\varepsilon \gg 1$. Finally, in figure 17(*b*) we verify the impulse response approximation (4.18) for the same three values of ε. We note that for perfect edge slip, substitution of expression (4.8) for the overall flux

https://doi.org/10.1017/jfm.2013.276 Published online by Cambridge University Press

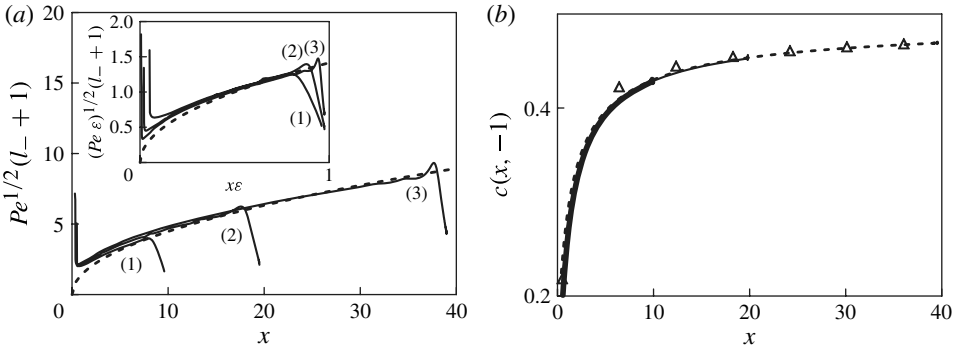


FIGURE 17. Surface convection in Couette circulation and SCL fine structure. $Pe\,\varepsilon = 25$, and $\varepsilon = 0.025, 0.05, 0.1$. (*a*) Normalized separatrices $y = (l_-(x) + 1)Pe^{1/2}$: (1) $\varepsilon = 0.025$, (2) $\varepsilon = 0.05$, (3) $\varepsilon = 0.1$; dashed line, approximation $y = \sqrt{2x}$. Inset: collapse of normalized separatrices for $y = (l_-(x\varepsilon) + 1)Pe^{1/2}$: (1), (2), (3) and the dashed line correspond to the same curves as in (*a*). (*b*) The wall concentration, $c(x, -1)$: bold solid line, $\varepsilon = 0.1$; solid line, $\varepsilon = 0.05$; dashed line, $\varepsilon = 0.025$; triangles, approximation $1/2 - 0.7\sqrt{1/4\pi x}$.

through the channel in (4.17) yields

$$c \approx \frac{1}{2} + 0.7 \begin{cases} -\sqrt{\dfrac{1}{4\pi x}}\,\mathrm{e}^{-Pe(y+1)^2/4x}, & 0 < y + 1 \ll 1, \\ \sqrt{\dfrac{1}{4\pi\left(\dfrac{1}{\varepsilon} - x\right)}}\,\mathrm{e}^{-Pe(y-1)^2/4(1/\varepsilon - x)}, & 0 < 1 - y \ll 1, \end{cases} \tag{4.19}$$

which implies the convergence of the wall concentration, $c(x, \pm 1)$, to its asymptotic form, independent of Pe and ε:

$$c \approx \frac{1}{2} + 0.7 \begin{cases} -\sqrt{\dfrac{1}{4\pi x}}, & y = -1, \\ \sqrt{\dfrac{1}{4\pi\left(\dfrac{1}{\varepsilon} - x\right)}}, & y = 1; \end{cases} \tag{4.20}$$

(4.20) is valid for $Pe\,\varepsilon \gg 1$ (figure 17*b*). Expression (4.20) explains the apparent paradox that the width of the SCL scales with $(Pe\,\varepsilon)^{-1/2}$ in the middle of the channel, apparently yielding the $Pe^{1/2}\varepsilon^{-1/2}$-scaling for the convective flux in the SCL. At the same time the width of the edge diffusion layer scales with $Pe^{-1/2}$ independently of ε, and thus N scales with $Pe^{1/2}$. This discrepancy in the flux scaling is resolved by the fact that, in accordance with (4.20), the deviation of the wall solute concentration from $1/2$ in the middle of the channel scales with $\varepsilon^{1/2}$.

In the surface convection regime the entire mass transfer through the channel is mediated by convection in SCLs. Their related redistribution of the mass flux may be traced via the following estimates. Let us consider a closed streamline, S_0, lying in the bulk and not passing through the edge diffusion layers and SCLs, $\Psi = \Psi_0 < 1$ (bold line in figure 5*c*). The region inside this streamline, $\Psi > \Psi_0$, affects the overall solute

https://doi.org/10.1017/jfm.2013.276 Published online by Cambridge University Press

flux through the channel only via the diffusion flux across the streamline. Disregarding the edge portion of our streamline, we may estimate this flux as $O(|\partial c/\partial y|)/\varepsilon)$. Considering the cross-section $x = x_0 \in (0, 1/\varepsilon)$ of the channel and using the flux balance in the stream-tube Ψ_0 $(0 < \Psi < \Psi_0)$ and neglecting the longitudinal diffusion contribution to the mass flux, we find that

$$|J(\Psi)| \leqslant Pe \int_{\{\Psi<\Psi_0\}\bigcap\{x=x_0\}} |y||c(x_0, y) - \overline{c}(x_0)|\,\mathrm{d}y \leqslant O(N), \tag{4.21}$$

where $-J(\Psi)$ is the contribution of the stream-tube Ψ to the total flux $-N$ through the channel (figure 5). Substituting the estimate (4.9) for the overall dimensionless flux N into (4.21), we obtain the following estimate for the deviation of the stream-tube concentration from its cross-section average $\overline{c}$:

$$|c - \overline{c}| \leqslant O\left(\frac{N}{Pe}\right) \leqslant O\left(Pe^{-1/2}\right). \tag{4.22}$$

Since outside the SCLs the variation of the concentration across the channel is related to its deviation from its cross-sectional average as

$$\left|\frac{\partial c}{\partial y}\right| = O(|c - \overline{c}|), \tag{4.23}$$

(4.22) implies that for $Pe\,\varepsilon \gg 1$ we have

$$\oint_{S_0} \left|\frac{\partial c}{\partial y}\right| \mathrm{d}S_0 \leqslant O\left(\left|\frac{\partial c}{\varepsilon \partial n}\right|\right) \leqslant O\left(\frac{1}{Pe^{1/2}\varepsilon}\right) = O\left(\frac{N}{Pe\,\varepsilon}\right), \tag{4.24}$$

that is, the diffusion flux through the selected streamline and thus the contribution of the bulk to the overall flux N are negligible in comparison. This estimate is just a variation of the Prandtl–Batchelor theorem (Prandtl 1904; Batchelor 1956; Acheson 1990) and the related results by Burggraf (1966) and Acrivos *et al.* (Acrivos & Goddard 1965; Goddard & Acrivos 1966; Pan & Acrivos 1968; Leal 2007).

As the last illustration of flux redistribution and a complement to figure 5(*b*), in the inset to figure 16(*d*) we present the normalized flux density profiles in the middle cross-section of the channel, computed for an increasing sequence of $Pe\,\varepsilon$.

To summarize, the same three regimes as in ZDCF may be distinguished in circulation too.

(i) $Pe \leqslant O(1)$: dominance of the TAD mechanism characterized by an efficient cross-diffusion averaging of the solute concentration over various streamlines.

(ii) $O(1) < Pe \leqslant O(1/\varepsilon)$: breakdown of TAD through the development of WFs. In terms of the elliptic or the two-way diffusion model, (3.2*a–d*) or (3.9*a–d*), respectively, this means the coexistence of the TAD solution with the exponential modes and the emergence near the channel edges of a lateral non-uniformity of the longitudinal concentration gradient, propagating along the channel.

(iii) $Pe\,\varepsilon \gg 1$: in this range, the WF reaches the opposite edge of the channel and turns into an $O((Pe\,\varepsilon)^{-1/2})$-wide SCL, heralding the onset of surface convection. Transition from TAD to the SCL regime is reflected by the transition from $N \sim Pe^2$ to $N \sim Pe^{1/2}$ dependence of the overall flux on the flow rate (figure 18), characteristic of convective transfer in a $(Pe\,\varepsilon)^{-1/2}$-wide SCL with a finite concentration.

https://doi.org/10.1017/jfm.2013.276 Published online by Cambridge University Press

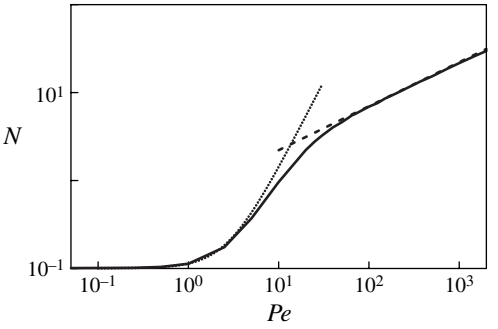


FIGURE 18. Transition from TAD to surface convection in Couette circulation. N versus Pe for $\varepsilon = 0.05$ (solid line) and its approximations by the TAD relation, $N = 2\varepsilon\left(2/15Pe^2 + 1\right)$ (dotted line, 2ε, unperturbed longitudinal concentration gradient), and by SCL square root dependence, $N = 0.7Pe^{1/2}$ (dashed line).

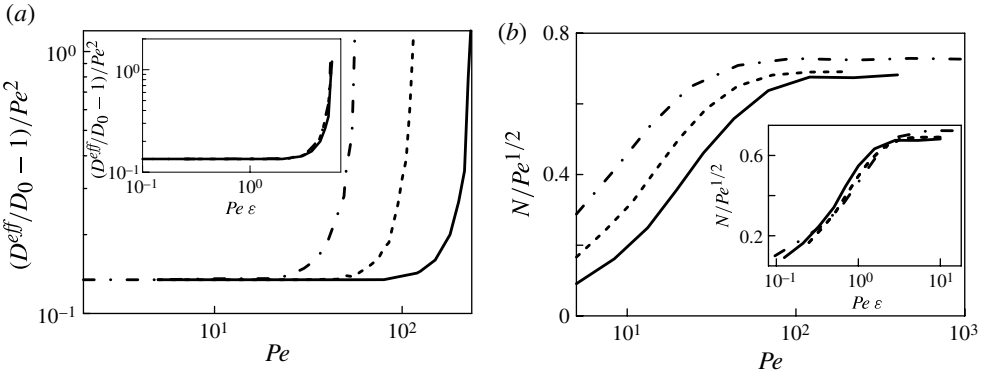


FIGURE 19. Breakdown of TAD and transition to surface convection in Couette circulation in terms of $Pe\,\varepsilon$. (*a*) $(D^{eff}/D_0 - 1)/Pe^2$ versus Pe in the middle of the channel for $\varepsilon = 0.025$ (solid line), $\varepsilon = 0.05$ (dashed line), $\varepsilon = 0.1$ (dot-dashed line). Inset: $(D^{eff}/D_0 - 1)/Pe^2$ versus $Pe\,\varepsilon$ for the same values of ε. (*b*) $N/Pe^{1/2}$ versus Pe for $\varepsilon = 0.025$ (solid line), $\varepsilon = 0.05$ (dashed line), $\varepsilon = 0.1$ (dot-dashed line). Inset: $N/Pe^{1/2}$ versus $Pe\,\varepsilon$ for the same values of ε.

To illustrate the role of $Pe\,\varepsilon$ as a crucial control parameter in circulation flow, in figure 19 we present plots analogous to those in figure 12 for ZDCF. Thus, in figure 19(*a*), we illustrate the breakdown of the TAD relation for the effective diffusivity, D^{eff}, as a function of Pe (for $\varepsilon = 0.025, 0.05, 0.1$) and of $Pe\,\varepsilon$, observing perfect collapse of the three curves. In addition, we illustrate the appearance of $Pe\,\varepsilon$ in the N versus Pe dependence depicted in figure 18, and we define the 'effective SCL concentration' as $N/Pe^{1/2}$. In figure 19(*b*) we plot $N/Pe^{1/2}$ as a function of Pe, for the same three values of ε as in figure 19(*a*), and observe a collapse in terms of $Pe\,\varepsilon$ once again.

This scenario also holds for Couette circulation with no-slip at the channel edges and for Poiseuille circulation. As previously mentioned, the no-slip at the edges yields a higher rate of the bulk mixing compared to perfect slip ((4.10), (4.11)). While the breakdown of TAD and transition to surface convection occur at a lower flow

https://doi.org/10.1017/jfm.2013.276 Published online by Cambridge University Press

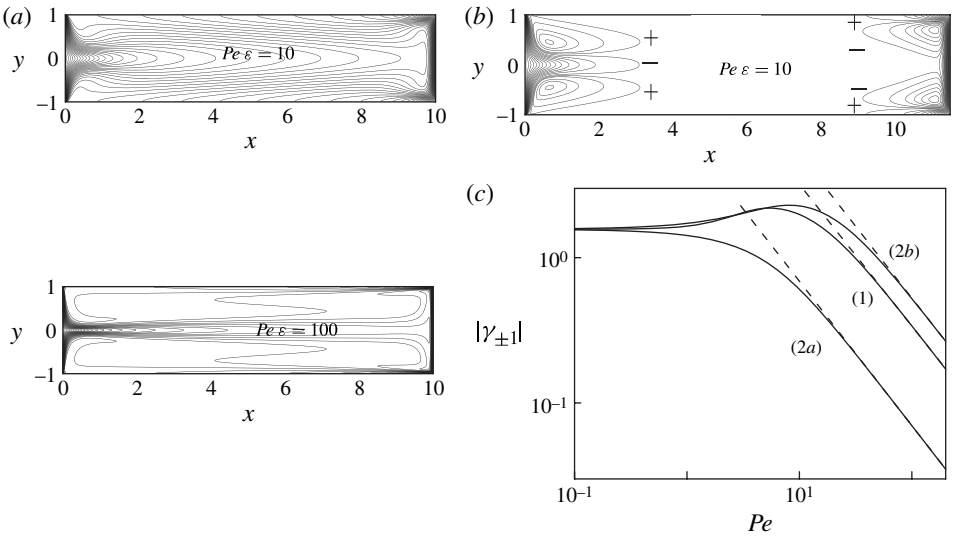


FIGURE 20. WFs and breakdown of TAD in Poiseuille circulation with perfect edge slip. (*a*) Concentration level lines for $Pe\,\varepsilon = 10, 100$. (*b*) Level lines of edge perturbations, Σ_1 and Σ_2 for $Pe\,\varepsilon = 10$; + positive and − negative deviations from TAD. (*c*) Exponential modes in Couette and Poiseuille flow: (1) $|\gamma_{\pm 1}|$ (solid line), $|\nu_{\pm}1|/Pe$ (dashed line) for Couette flow; (2*a*) leading exponential for the depleted edge in Poiseuille flow, $-\gamma_1$ (solid line), $-\nu_1/Pe$ (dashed line); (2*b*) leading exponential for the enriched edge, γ_{-1} (solid line), ν_{-1}/Pe (dashed line).

rate for no-slip compared to perfect slip, the hydrodynamic conditions at the channel edges do not affect the characteristic ranges for all three regimes. Thus, with edge no-slip, the expressions (4.18) for the shape of the SCL, $l_{\pm}(x)$, remain valid. In addition, the general form of the concentration profile (4.19) remains valid too, with only the 0.7-prefactor replaced by the one proportional to $Pe^{-1/6}$, in accordance with the flux scaling (4.7). The main peculiarity of Poiseuille flow is the asymmetry of the downstream slip flow and the pressure-driven back flow. Accounting for this asymmetry results in a faster development of WFs along the channel axis in the exiting flow at the depleted edge, $x = 0$, compared to that at the enriched edge, $x = 1/\varepsilon$, as illustrated in figure 20.

5. Spiral pattern and fine structure of SCL

In this last section we address the surface convection regime, $Pe\,\varepsilon \gg 1$, analysing the fine structure of the SCL and pondering the bulk after it has been nearly excluded from the mass transfer through the channel. We limit ourselves to the most symmetrical case of Couette flow with perfect slip at the edges. The main peculiarity of the surface convection regime in circulation is the formation of a spiral concentration pattern (figures 6*d*, 16*a*). In figure 21 we illustrate the transformation of the average concentration level line, $c(x, y) = 0.5$, from a straight line $x = 1/(2\varepsilon)$, for $Pe = 0$, into a zigzagged curve and a spiral with increasing number of loops with increase in $Pe\,\varepsilon$. Evaluating the width of a spiral loop, we note for $Pe\,\varepsilon \gg 1$ the appearance of the scale $y \sim (Pe\,\varepsilon)^{-1/2}$ (constant width of the white/grey stripe of a spiral loop for a given value of $Pe\,\varepsilon$, for various Pe and ε, in the four bottom rows

https://doi.org/10.1017/jfm.2013.276 Published online by Cambridge University Press

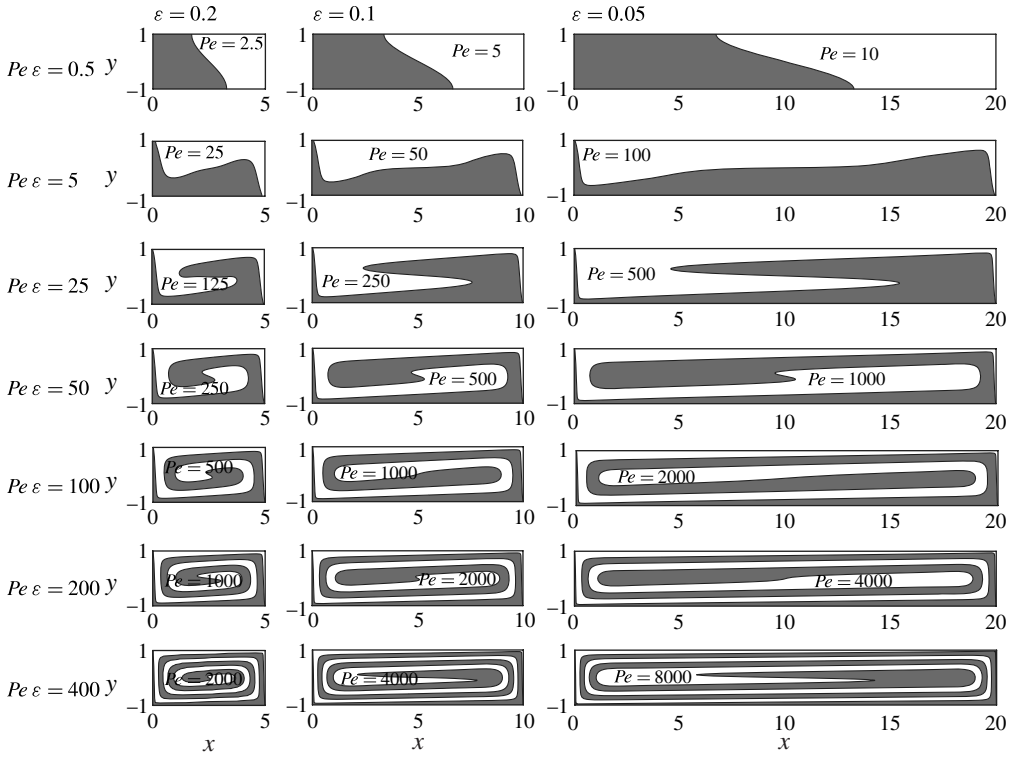


FIGURE 21. Spiral pattern in Couette circulation. Concentration level line, $c(x, y) = 0.5$, for $Pe\,\varepsilon = 0.5, 5, 25, 50, 100, 200, 400$ and $\varepsilon = 0.05, 0.1, 0.2$ (white colour, enrichment, $c(x, y) > 0.5$; grey, depletion, $c(x, y) < 0.5$.

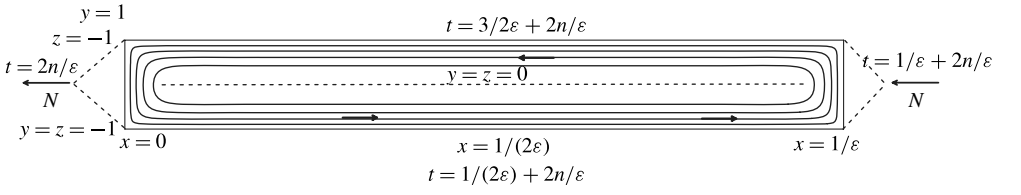


FIGURE 22. Sketch of transition to Lagrange variables in Couette circulation.

in figure 22, corresponding to the spiral regime) which agrees with the previously observed $(Pe\,\varepsilon)^{-1/2}$-scaling for the separatrices, $y = l_{\pm}(x)$ (figure 17*a*).

We are unable to analytically trace the spiral concentration pattern directly in model (4.1*a–d*). This motivates us to look for an even simpler model admitting an analytical treatment and retaining the basic characteristic features of (4.1*a–d*), such as the angular periodicity of circulation and the plane-parallel character of the flow in the bulk of the channel. With this in mind, let us rewrite the problem (4.1*a–d*) in Lagrange variables, (ψ, t), following Pan & Acrivos (1968) and Leal (2007). Here, t varies along the streamline, $\psi = \text{const}$. We recall that for Couette circulation in the

https://doi.org/10.1017/jfm.2013.276 Published online by Cambridge University Press

bulk of the channel where the flow is plane-parallel, ψ is given by

$$\psi = \frac{1-y^2}{2}. \tag{5.1}$$

To simplify this transform, we restrict ourselves to considering the bulk of the channel away from the edges, neglect the longitudinal diffusion (first term on the right-hand side of (4.1*a*)), and replace the rectangular channel by a cigar-like one, with edges contracted to point-like tips (figure 22) with finite mass fluxes N going through them. To preserve the form of the bulk diffusion equation (3.9*a*), we rescale the transversal variable ψ in the bulk of the channel, (5.1), and replace it by z defined by

$$z = -\sqrt{1-2\psi} = -|y|. \tag{5.2}$$

Finally, the longitudinal variable t for a cigar-like channel may be defined by

$$t = -x \operatorname{sign} y. \tag{5.3}$$

In new coordinates the circulation loop is transformed into a unidirectional flow (see figure 22 for illustration) with the channel transformed into an infinite horizontal strip of width unity, in which the concentration $c(z,t)$ obeys the one-way diffusion analogue of (4.1*a*) (recall once more (2.5), (3.9*a*)), of the form

$$-Pez\frac{\partial c}{\partial t} = \frac{\partial^2 c}{\partial z^2}, \quad -1 < z < 0, -\infty < t < \infty. \tag{5.4}$$

Here the top boundary of the strip, $z = 0$, corresponds to the axis of the channel, whereas the bottom boundary, $z = -1$, corresponds to an infinite periodic sequence of alternating channel walls and edges, with

$$z = -1, \quad t = \frac{2n+1}{2\varepsilon} \quad \text{middle-point of channel wall,} \tag{5.5a}$$

$$z = -1, \quad t = \frac{2n+1}{\varepsilon} \quad \text{enriched edge with a pulse-like mass flux } N \text{ entering the strip,} \tag{5.5b}$$

$$z = -1, \quad t = \frac{2n}{\varepsilon} \quad \text{depleted edge with a pulse-like mass flux } N \text{ exiting the strip,} \tag{5.5c}$$

$$z = -1, \quad \frac{n}{\varepsilon} < t < \frac{n+1}{\varepsilon} \quad \text{insulated channel wall,} \tag{5.5d}$$

for $n = 0, \pm 1, \pm 2 \ldots$. At this boundary $z = -1$ we specify the mass flux density via the following singular Neumann condition:

$$c_z(-1,t) = (-1)^n N\delta\left(t - \frac{n}{\varepsilon}\right), \quad n = 0, \pm 1, \pm 2 \ldots. \tag{5.6}$$

At the equivalent of the channel axis, $z = 0$, we enforce the continuity of c and $\partial c/\partial y$ by imposing the following non-local boundary conditions, pertaining to the suitable axis points in the forward and back flow portions of circulation. This yields

$$c\left(0, t + \frac{2n}{\varepsilon}\right) = c\left(0, -t + \frac{2n}{\varepsilon}\right), \tag{5.7}$$

$$c_z\left(0, t + \frac{2n}{\varepsilon}\right) = -c_z\left(0, -t + \frac{2n}{\varepsilon}\right), \quad t \neq \frac{n}{\varepsilon}, \ n = 0, \pm 1, \pm 2 \ldots. \tag{5.8}$$

https://doi.org/10.1017/jfm.2013.276 Published online by Cambridge University Press

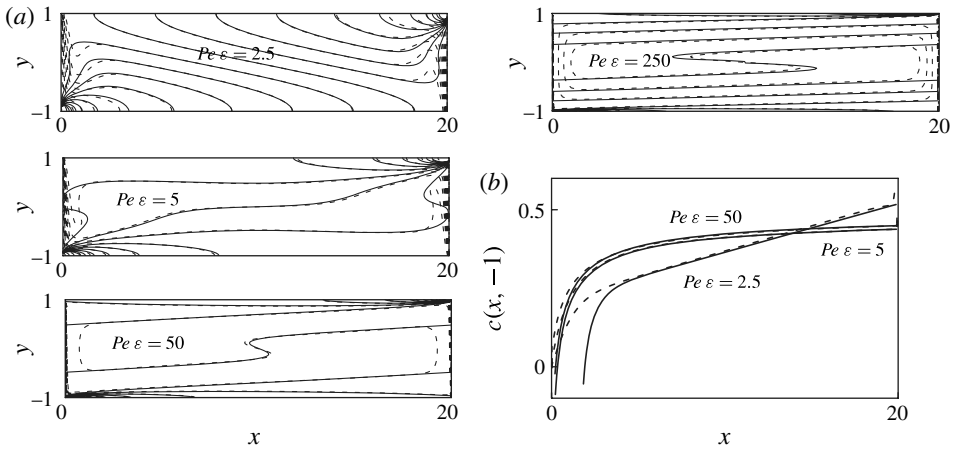


FIGURE 23. Couette circulation and periodic diffusion model (numerical solution of (4.1*a–d*), dashed line, and (5.4)–(5.9), solid line). (*a*) Concentration level lines (solution to (5.4)–(5.9) folded back via returning to the Cartesian coordinates, $(t, z) \to (x, y)$). (*b*) Depleted wall concentration, $c(x, -1)$.

To complete the formulation, we fix the average concentration at one half:

$$\int_{-1}^{0}\int_{0}^{2/\varepsilon} (c(z,t) - 0.5)\,\mathrm{d}t\,\mathrm{d}z = 0. \tag{5.9}$$

While the solution to the 'time-periodic' diffusion model (5.4)–(5.9) is unbounded near the equivalents of the channel edges, $t = n/\varepsilon$, $z = -1, n = \pm 1, \pm 2\ldots$, for $Pe \gg 1$ and small ε, it is in fairly good agreement with the numerical solution of the original problem (4.1*a–d*) away from the edges, reproducing, in particular, the WF growth and the separatrix of the previous section (figure 23*a,b*).

To trace the spiral formation analytically we expand $c(z, t)$ into Fourier series in t:

$$c(z,t) = 0.5 + 2\varepsilon N \sum_{n=1}^{\infty} (A_n(z)\cos(\pi\varepsilon n t) + B_n(z)\sin(\pi\varepsilon n t)). \tag{5.10}$$

Substitution of (5.10) in (5.4) yields

$$\frac{\mathrm{d}^2 A_n}{\mathrm{d}z^2} = -\pi Pe\,\varepsilon n z B_n, \quad \frac{\mathrm{d}^2 B_n}{\mathrm{d}z^2} = \pi Pe\,\varepsilon n z A_n, \quad -1 < z < 0. \tag{5.11}$$

Substitution of (5.10) into Fourier series expansion of the boundary condition (5.6) yields

$$\frac{\mathrm{d}A_n}{\mathrm{d}z}(-1) = \begin{cases} 0, & n = 2l, l = 1, 2\ldots, \\ 1, & n = 2l-1, l = 1, 2\ldots, \end{cases} \quad \frac{\mathrm{d}B_n}{\mathrm{d}z}(-1) = 0, \tag{5.12}$$

whereas applying continuity conditions (5.7), (5.8) provides the boundary conditions

$$\frac{\mathrm{d}A_n}{\mathrm{d}z}(0) = 0, \quad B_n(0) = 0, \tag{5.13}$$

thus completing the formulation of the boundary value problem (5.11)–(5.13) for $A_n(z)$, $B_n(z)$. The oddness of the Neumann condition (5.6) yields vanishing of the even-

https://doi.org/10.1017/jfm.2013.276 Published online by Cambridge University Press

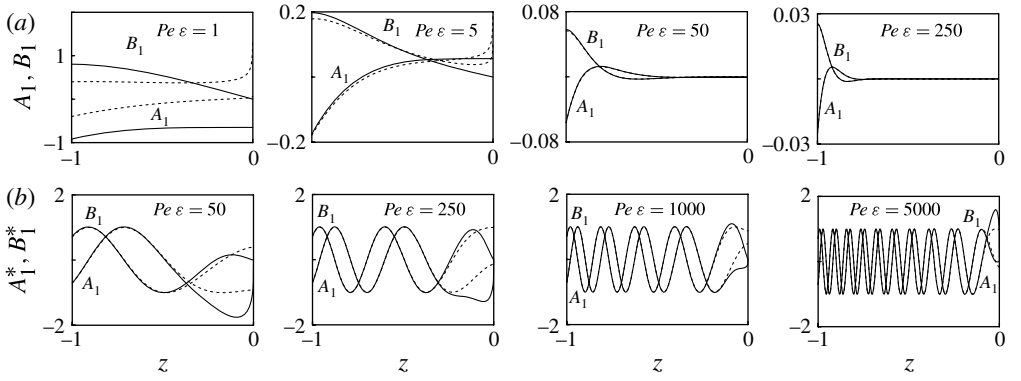


FIGURE 24. Leading-order coefficients, A_1 and B_1, in the periodic model. (*a*) $A_1(z)$ and $B_1(z)$ (solid line) and their approximation by (5.14), (5.15) (dashed line) for $Pe\,\varepsilon = 1, 5, 50, 250$. (*b*) Number of roots (spiral loops) increasing with $Pe\,\varepsilon$. Normalized $A_1^* = A_1(z)\exp(\sqrt{2\pi Pe\,\varepsilon}(1 - (-z)^{3/2})/3)(\pi Pe\,\varepsilon\sqrt{-z})^{1/2}$ and $B_1^* = -B_1(z)\exp(\sqrt{2\pi Pe\,\varepsilon}(1 - (-z)^{3/2})/3)(\pi Pe\,\varepsilon\sqrt{-z})^{1/2}$ (solid line) and their approximation by $\cos(\pi/4 - \sqrt{2\pi Pe\,\varepsilon}((-z)^{3/2} - 1)/3)$ and $\sin(\pi/4 - \sqrt{2\pi Pe\,\varepsilon}((-z)^{3/2} - 1)/3)$ (dashed line), for $Pe\,\varepsilon = 50, 250, 1000, 5000$.

indexed coefficients $A_n(z)$, $B_n(z)$, whereas for odd indices the problem (5.11)–(5.13) can be solved in terms of Airy functions (figure 24). Moreover, approximating the corresponding Airy functions by their asymptotics at infinity, we obtain for $Pe\,\varepsilon \gg 1$

$$A_1 \approx \exp\left(\frac{\sqrt{2\pi Pe\,\varepsilon}}{3}((-z)^{3/2} - 1)\right)\left(\pi Pe\,\varepsilon\sqrt{-z}\right)^{-1/2} \times \cos\left(\frac{\pi}{4} - \frac{\sqrt{2\pi Pe\,\varepsilon}}{3}((-z)^{3/2} - 1)\right), \tag{5.14}$$

$$B_1 \approx -\exp\left(\frac{\sqrt{2\pi Pe\,\varepsilon}}{3}((-z)^{3/2} - 1)\right)\left(\pi Pe\,\varepsilon\sqrt{-z}\right)^{-1/2} \times \sin\left(\frac{\pi}{4} - \frac{\sqrt{2\pi Pe\,\varepsilon}}{3}((-z)^{3/2} - 1)\right), \tag{5.15}$$

valid away from the equivalent of the channel axis, $z = 0$ (figure 24*b*). Since by (5.11) A_n and B_n are identical to A_1 and B_1 upon re-normalization of $Pe\,\varepsilon$ by n, approximations analogous to (5.14), (5.15) also hold for $n = 3, 5\ldots$. Equations (5.14) and (5.15) yield exponential vanishing of the Fourier coefficients A_n, B_n, $n = 1, 3, 5\ldots$ in the bulk, $z > -1$, with increase $Pe\,\varepsilon$ and imply fast convergence to one half of concentration away from the wall. We note that for any finite $z > 0$ the distance between the roots of A_1, B_1 (width of a spiral loop) scales with $(Pe\,\varepsilon)^{-1/2}$ and so does the decay rate of amplitude towards the channel axis. Substitution of (5.14), (5.15) into (5.10) yields for $Pe\,\varepsilon \gg 1$ the following representation of solute concentration in the form of superposition of terms, which is reminiscent of thermal waves in heat

https://doi.org/10.1017/jfm.2013.276 Published online by Cambridge University Press

conductance (Ångström 1861; Carslaw 1921; Samarskii & Tikhonov 1961):

$$c(z,t) = 0.5 + 2\varepsilon N \sum_{n=1,3,5\ldots} \exp\left(\frac{\sqrt{2\pi Pe\,\varepsilon n}}{3}((-z)^{3/2}-1)\right)\left(\pi Pe\,\varepsilon n\sqrt{-z}\right)^{-1/2} \times \cos\left(\pi\varepsilon n t + \frac{\pi}{4} - \frac{\sqrt{2\pi Pe\,\varepsilon n}}{3}((-z)^{3/2}-1)\right). \tag{5.16}$$

As mentioned earlier, all spiral loops except for the first one, adjacent to the wall, are dominated by the leading-order non-constant mode, $n = 1$, whereas the first loop is affected by all periodic modes in accordance with (5.16). Keeping the leading-order mode in (5.16), linearizing it in z in the vicinity of the wall, and equating c to one half, we infer the $(Pe\,\varepsilon)^{-1/2}$-scaling, reported in the previous section (figure 17*a*).

Similar conclusions also hold for Poiseuille circulation. Nevertheless, due to the numerous technicalities involved in a systematic generalization of the above analysis to Poiseuille circulation, we skip it here.

To summarize, in this study we used two types of expansion for solute concentration. The one in exponential diffusion modes, (3.15), (3.16), was suitable for modelling the edge/wall interaction at moderate/low $Pe\,\varepsilon$ as expressed in the emergence and growth of WFs, the related breakdown of TAD, emergence of SCLs and transition to surface convection. The other 'thermal wave' expansion, (5.10), (5.16), is suitable for modelling the periodic elements in circulation for large $Pe\,\varepsilon$, such as the spiral pattern determining the fine structure of SCLs and the bulk. The latter is dominated by the first non-constant mode in (5.10) since the higher-order modes decay in the transversal direction much more rapidly. The equivalence of these two expansions is illustrated by reproducing the moderate/low $Pe\,\varepsilon$ phenomenology using the periodic expansion (5.10). Thus, in figure 25 we show how, for $Pe\,\varepsilon \leqslant O(1)$, accounting for the higher-order modes in (5.10) allows us to trace the WF formation and the appearance of a separatrix previously modelled by (3.15), (3.16).

6. Conclusions

In a circulatory flow, for low Pe numbers, mass transport along the channel is controlled by three diffusion resistances in series: those of the edge diffusion boundary layers and that of the bulk. Resistance of the former depends on their width and that of the latter is controlled by the TAD mechanism. Each element affects the others through its contribution to determining the solute concentration at the edge of the neighbouring element. Upon increase in Pe, the boundary layers shrink; accordingly, their resistances decrease, and so does the effective bulk resistance, albeit the latter faster than those of the boundary layers. For some finite value of Pe, dependent on the channel aspect ratio, the bulk resistance vanishes. Paradoxically, at this point transport through the bulk effectively ceases, short-circuited by the convective surface transport along the channel sidewalls in SCLs. These latter develop from WFs and SWFs which emerge through the streamline mapping of the upstream edge diffusion layers onto the channel walls. WFs and SWFs grow upon increase in Pe via a diffusion-like mechanism. Their growth is accompanied by the breakdown of the TAD regime along the channel via the development of transversal non-uniformities of axial concentration gradient. Once a WF's tip reaches the opposite channel edge, an SCL is formed and the surface convection regime sets in. Upon further increase in Pe, concentration distribution in SCLs (and the bulk) acquires its spiral character.

https://doi.org/10.1017/jfm.2013.276 Published online by Cambridge University Press

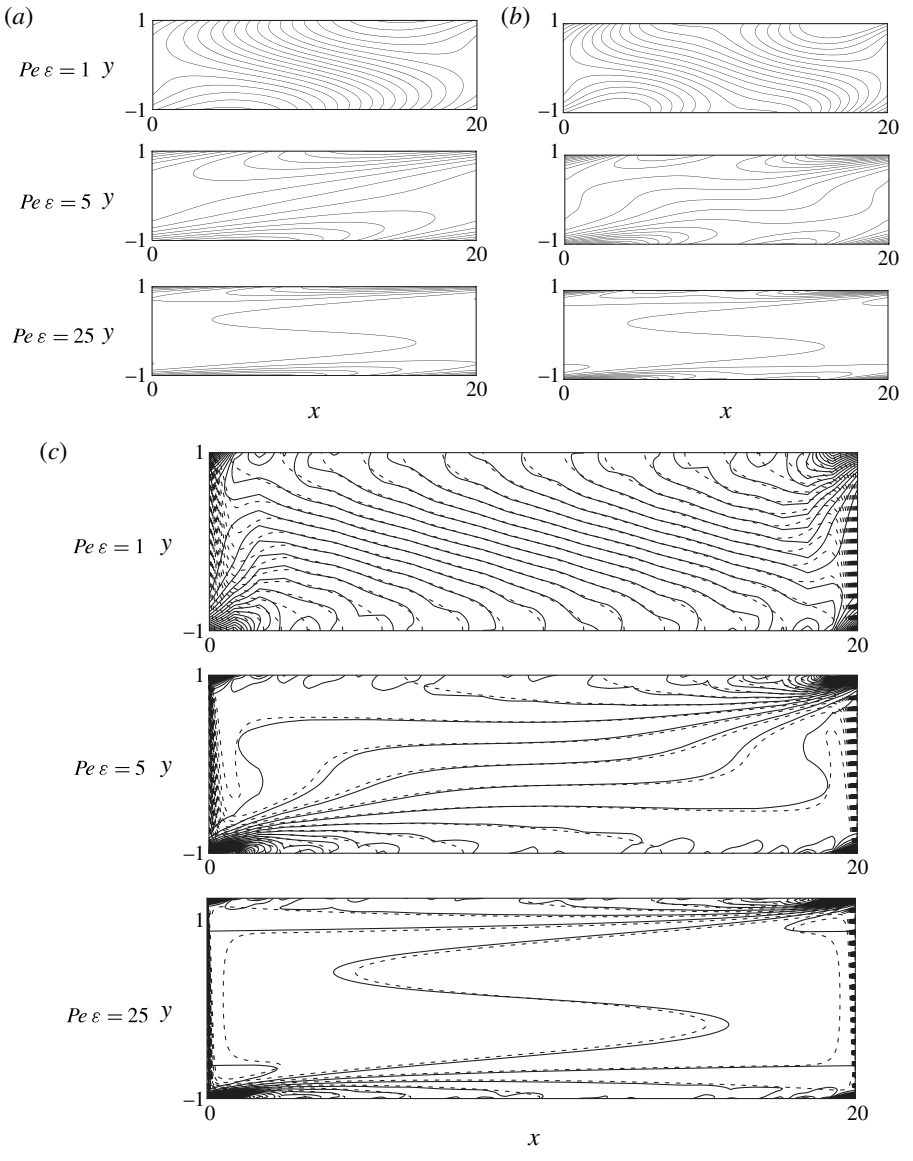


FIGURE 25. Concentration level lines for truncated Fourier series approximation, $c(z,t) = 0.5 + 2\varepsilon N\sum_1^k (A_n(z)\sin(\pi\varepsilon nt) + B_n(z)\cos(\pi\varepsilon nt))$ for $Pe\,\varepsilon = 1, 5, 25$: (*a*) $k = 1$, (*b*) $k = 4$, (*c*) $k = 18$. Solid line, approximation; dashed line, numerical solution of (4.1*a–d*).

Summarizing, the three essentials of mass transfer in our system are:

(i) co-presence and interaction of open channel edges (fixed edge concentrations) and insulated sidewalls (no-flux conditions);

(ii) periodicity, related to circulation;

(iii) capture of the most essential elements by the diffusion-like parabolic limit (the limiting two-way diffusion (2.5), (3.9*a*) or (5.4) compared to the full elliptic convection–diffusion equation (2.3*a*) or (3.4*a*).

https://doi.org/10.1017/jfm.2013.276 Published online by Cambridge University Press

The first of the three determines the development of WFs, the related breakdown of TAD, the stabilization of wall concentration, and the development of SCLs. The second, hidden at slow circulations, reaches its ultimate expression in the spiral pattern underlying the fine structure of wall SCLs at large circulation velocities. Finally, the third provides a convenient tool for studying the first two, capturing most of the events occurring upon increase in *Pe*, with elliptic elements mattering only for details (e.g. solute distribution near the channel corners and the matching of the 'diffusional' concentration with the constant boundary value across the 'dense' downstream portion of the edge diffusion layer).

In terms of CP and over-limiting conductance which motivated this study, transition to surface convection may be important as a source of formation of lateral electrolyte concentration variations in the channel. The latter, combined with a longitudinal electric field, inducing the circulation, may be the source of recently reported secondary vortical flow in the channel (Kim *et al.* 2012; M. Z. Bazant, private communication). Flow of this kind could result from electrokinetic instability expected in the setups with electric field normal to conductivity gradient (Lin *et al.* 2004; Chen *et al.* 2005).

Acknowledgement

The work was supported by the USA–Israel Binational Science Foundation (grant 2010199).

REFERENCES

ACHESON, D. J. 1990 *Elementary Fluid Dynamics*, 1st edn. Oxford University Press.

ACRIVOS, A. & GODDARD, J. D. 1965 Asymptotic expansions for laminar forced-convection heat and mass transfer. *J. Fluid Mech.* **23**, 273–291.

ÅNGSTRÖM, A. J. 1861 Neue Methode das Wärmeleitungsvermögen der Körper zu bestimmen. *Ann. Phys. Chem.* **114**, 513–530.

ARIS, R. 1956 On the dispersion of a solute in a fluid flowing through a tube. *Proc. R. Soc. Lond.* A **235**, 67–77.

BALAKOTAIAH, V. & CHANG, H.-C. 1995 Dispersion of chemical solutes in chromatographs and reactors. *Phil. Trans. Roy. Soc. Lond.* A **351**, 39–75.

BALAKOTAIAH, V. & CHANG, H.-C. 2003 Hyperbolic homogenized models for thermal and solutal dispersion. *SIAM J. Appl. Maths* **63**, 1231–1258.

BATCHELOR, G. K. 1956 On steady laminar flow with closed streamlines at large Reynolds number. *J. Fluid Mech.* **1**, 177–190.

BAZANT, M. Z., DYDEK, E. V., DENG, D. S. & MANI, A. 2011 Method and apparatus for desalination and purification. *US Patent Application* **2011**, 0308953.

BEALS, R. 1981 Partial-range completeness and existence of solutions to two-way diffusion equations. *J. Math. Phys.* **22**, 954–960.

BEALS, R. 1985 Indefinite Sturm–Liouville problems and half-range completeness. *J. Differ. Equ.* **56**, 391–407.

BRENNER, H. & EDWARDS, D. A. 1993 *Macrotransport Processes*, 1st edn. Butterworth–Heinemann.

BURGGRAF, O. 1966 Analytical and numerical studies of the structure of steady separated flows. *J. Fluid Mech.* **24**, 113–151.

CARSLAW, H. S. 1921 *Introduction to the Mathematical Theory of the Conduction of Heat in Solids*, 2nd edn. Macmillan.

CHAMARTHY, P., KUMAR, A., CAO, J. & WERELEY, S. T. 2008 Fundamentals of diffusion in microfluidic systems. In *Encyclopedia of Microfluidics and Nanofluidics* (ed. D. Li), pp. 761–768. Springer.

https://doi.org/10.1017/jfm.2013.276 Published online by Cambridge University Press

CHANG, H.-C. & YEO, L. 2009 *Electrokinetically Driven Microfluidics and Nanofluidics*, 1st edn. Cambridge University Press.

CHEN, C. H., LIN, H., LELE, S. K. & SANTIAGO, J. G. 2005 Convective and absolute electrokinetic instability with conductivity gradients. *J. Fluid Mech.* **524**, 263–303.

DYDEK, E. V., ZALTZMAN, B., RUBINSTEIN, I., DENG, D. S., MANI, A. & BAZANT, M. Z. 2011 Overlimiting current in a microchannel. *Phys. Rev. Lett.* **107**, 118301.

GODDARD, J. D. & ACRIVOS, A. 1966 Asymptotic expansions for laminar forced-convection heat and mass transfer. Part 2. Boundary-layer flows. *J. Fluid Mech.* **24**, 339–366.

GRAETZ, L. 1882 Über die Wärmeleitungsfähigkeit von Flüssigkeiten. *Ann. Phys.* **254**, 79–94.

KIM, S. J., KO, S. H., KANG, K. H. & HAN, J. 2010 Direct seawater desalination by ion concentration polarization. *Nat. Nanotech.* **5**, 297–301.

KIM, S. J., KO, S. H., KWAK, R., POSNER, J. D., KANG, K. H. & HAN, J. 2012 Multi-vortical flow inducing electrokinetic instability in ion concentration polarization layer. *Nanoscale* **4**, 7406–7410.

LEAL, L. G. 2007 *Advanced Transport Phenomena*, 1st edn. Cambridge University Press.

LIN, H., STOREY, B., ODDY, M., CHEN, C. H. & SANTIAGO, J. G. 2004 Instability of electrokinetic microchannel flows with conductivity gradients. *Phys. Fluids* **16**, 1922–1935.

MANI, A. & BAZANT, M. Z. 2011 Deionization shocks in microstructures. *Phys. Rev.* E **84**, 061504.

MANI, A., ZANGLE, T. A. & SANTIAGO, J. G. 2009 On the propagation of concentration polarization from microchannel–nanochannel interfaces. Part 1. Analytical model and characteristic analysis. *Langmuir* **25**, 3898–3908.

NUNGE, R. J. & GILL, W. N. 1966 An analytical study of laminar counterflow double-pipe heat exchangers. *AIChE J.* **12**, 279–289.

PAN, F. U. & ACRIVOS, A. 1968 Heat transfer at high Péclet numbers in regions of closed streamlines. *Intl J. Heat Mass Transfer* **11**, 439–444.

PRANDTL, L. 1905 Über Flüssigkeitsbewegung bei sehr kleiner Reibung. In *Verhandlungen d. III. Internat. Math. Kongr. Heidelberg, 8–13 Aug. 1904*, pp. 484–491. B. G. Teubner.

RUBINSTEIN, I. & SHTILMAN, L. 1979 Voltage against current curves of cation exchange membranes. *J. Chem. Soc. Faraday Trans.* **75**, 231–246.

RUBINSTEIN, I. & ZALTZMAN, B. 2000 Electro-osmotically induced convection at a permselective membrane. *Phys. Rev.* E **62**, 2238–2251.

RUBINSTEIN, I. & ZALTZMAN, B. 2010 Dynamics of extended space charge in concentration polarization. *Phys. Rev.* E **81**, 061502.

RUBINSTEIN, I., ZALTZMAN, B., PRETZ, J. & LINDER, C. 2002 Experimental verification of the electroosmotic mechanism of overlimiting conductance through a cation exchange electrodialysis membrane. *Russ. Electrochem.* **38**, 853–864.

RUBINSTEIN, S. M., MANUKYAN, G., STAICU, A., RUBINSTEIN, I., ZALTZMAN, B., LAMMERTINK, R. G. H., MUGELE, F. & WESSLING, M. 2008 Direct observation of a nonequilibrium electro-osmotic instability. *Phys. Rev. Lett.* **101**, 236101.

SAMARSKII, A. A. & TIKHONOV, A. N. 1961 *Partial Differential Equations of Mathematical Physics*, 1st edn. Courier Dover.

STONE, H. A. & BRENNER, H. 1999 Dispersion in flows with streamwise variations of mean velocity: radial flow. *Ind. Engng Chem. Res.* **38**, 851–854.

TAYLOR, G. I. 1953 Dispersion of soluble matter in solvent flowing slowly through a tube. *Proc. R. Soc. Lond.* A **219**, 186–203.

YAROSHCHUK, A., ZHOLKOVSKIY, E., POGODIN, S. & BAULIN, V. 2011 Coupled concentration polarization and electroosmotic circulation near micro/nanointerfaces: Taylor–Aris model of hydrodynamic dispersion and limits of its applicability. *Langmuir* **27**, 11710–11721.

YOSSIFON, G. & CHANG, H. C. 2008 Selection of non-equilibrium overlimiting currents: universal depletion layer formation dynamics and vortex instability. *Phys. Rev. Lett.* **101**, 254501.

ZALTZMAN, B. & RUBINSTEIN, I. 2007 Electro-osmotic slip and electroconvective instability. *J. Fluid Mech.* **579**, 173–226.

ZANGLE, T. A., MANI, A. & SANTIAGO, J. G. 2009 On the propagation of concentration polarization from microchannel–nanochannel interfaces. Part 2. Numerical and experimental study. *Langmuir* **25**, 3909–3916.

https://doi.org/10.1017/jfm.2013.276 Published online by Cambridge University Press